EXPERIMENTAL AND NUMERICAL FAILURE ANALYSIS OF ADVANCED COMPOSITE STRUCTURES WITH HOLES

A THESIS SUBMITTED TO
THE GRADUATE SCHOOL OF NATURAL AND APPLIED SCIENCES
OF
MIDDLE EAST TECHNICAL UNIVERSITY

BY

MEHMET BİLAL ATAR

IN PARTIAL FULFILLMENT OF THE REQUIREMENTS
FOR
THE DEGREE OF MASTER OF SCIENCE
IN
MECHANICAL ENGINEERING

SEPTEMBER 2016

Approval of thesis:

EXPERIMENTAL AND NUMERICAL FAILURE ANALYSIS OF ADVANCED COMPOSITE STRUCTURES WITH HOLES

submitted by **MEHMET BİLAL ATAR** in partial fulfillment of the requirements for the degree of **Master of Science in Mechanical Engineering Department, Middle East Technical University** by,

Prof. Dr. Gülbin Dural Ünver _____
Dean, Graduate School of **Natural and Applied Sciences**

Prof. Dr. Tuna Balkan _____
Head of Department, **Mechanical Engineering**

Prof. Dr. K. Levend Parnas _____
Supervisor, **Mechanical Engineering Dept., TED Univ.**

Examining Committee Members:

Prof. Dr. F. Suat Kadıoğlu _____
Mechanical Engineering Dept., METU

Prof. Dr. Levend Parnas _____
Mechanical Engineering Dept., TED Univ.

Prof. Dr. Hakan I. Tarman _____
Mechanical Engineering Dept., METU

Asst. Prof. Dr. Hüsnü Dal _____
Mechanical Engineering Dept., METU

Prof. Dr. K. Müfit Gülgeç _____
Mechatronic Engineering Dept., Cankaya Univ.

Date: 21.09.2016

I hereby declare that all information in this document has been obtained and presented in accordance with academic rules and ethical conduct. I also declare that, as required by these rules and conduct, I have fully cited and referenced all material and results that are not original to this work.

Name, Last name: Mehmet Bilal Atar

Signature:

ABSTRACT

EXPERIMENTAL AND NUMERICAL FAILURE ANALYSIS OF ADVANCED COMPOSITE STRUCTURES WITH HOLES

Atar, Mehmet Bilal

M.Sc., Department of Mechanical Engineering

Supervisor: Prof. Dr. K. Levend Parnas

September 2016, 105 pages

In this work, a design methodology for advanced composite structures with holes is presented. A three dimensional finite element model (FEM) is constructed to simulate such a structural application similar to weight-pockets in helicopter blades. Material properties are obtained by a material characterization study. The progressive failure method with FEM is used for the material degradation. In order to induce delamination in simulation, cohesive layers are implemented between composite layers. Results are compared for sudden and progressive failure. Experiments are also conducted and the optimum computational approach to predict failure in such structures is discussed.

Key words: Composite Structures, Finite Element Method, Cohesive Zone Method, Progressive Failure

ÖZ

DELİKLİ İLERİ KOMPOZİT YAPILARIN DENEYSEL VE NUMERİK HASAR ANALİZİ

Atar, Mehmet Bilal

Yüksek Lisans, Makina Mühendisliği Bölümü

Tez Yöneticisi: Prof. Dr. K. Levend Parnas

Eylül 2016, 105 sayfa

Bu çalışmada, üzerinde delik bulunan kompozit yapılar için bir tasarım yöntemi sunulmaktadır. Bu çalışmada delikli kompozit yapılarda ve özellikle helikopter pallerindeki yük ceplerini simule etmek için üç boyutlu bir sonlu elemanlar modeli oluşturulmuştur. Sonlu elemanlar modelinde kullanılan malzeme özellikleri, bir malzeme karaterizasyonu çalışmasıyla belirlenmiştir. Yapısal hasarın simülasyonu için ilerlemeli hasar yöntemi kullanılmıştır. Delaminasyon hasarını belirlemek için tabakalar arasına yapışkan ara eleman eklenmiştir. Ani ve ilerlemeli hasar yaklaşımlarının sonuçları karşılaştırılmıştır. Yapılan deneylerle elde edilen sonuçlar simülasyon ile karşılaştırılmış ve bu tür yapılardaki hasar tespiti için en uygun sonlu elemanlar modeli tartışılmıştır.

Anahtar kelimeler: Kompozit Yapılar, Sonlu Elemanlar Yöntemi, Yapışkan Ara Eleman, İlerlemeli Hasar Analizi

ACKNOWLEDGEMENTS

First of all, I would like to express my gratitude to my supervisor Prof. Dr. K. Levend Parnas for his guidance and support through my undergraduate and graduate studies.

I would like to thank my colleagues Ozan Erartsın and Muhammed Çakır for sharing their knowledge and their support.

I also would like to thank Servet Şehirli and Mehmet Erili for their help in performing the tests.

This study is a part of SANTEZ project (960-STZ-2011-2) “Design Methodology for Thick Composite Laminates” which is supported by The Ministry of Science, Industry and Technology and Turkish Aerospace Industries (TAI).

TABLE OF CONTENTS

LIST OF TABLES

LIST OF FIGURES

NOMENCLATURE

Abbreviations

3D	Three Dimensional
ASTM	American Society for Testing Materials
CC	Compliance Calibration
CT	Compact Tension
CZM	Cohesive Zone Model
DCB	Double Cantilever Beam
DIN	Deutsches Institut für Normung
DL	Delamination
ENF	End Notched Flexure
ES	Element Size
FEM	Finite Element Model
FF	Fiber Failure
FPF	First Ply Failure
FRP	Fiber Reinforced Polymers
LTFE	Longitudinal Tension Fracture Energy
LCFE	Longitudinal Compression Fracture Energy
MBT	Modified Beam Theory
MCC	Modified Compliance Calibration
MF	Matrix Failure

MSM	Maximum Specific Modulus
MSS	Maximum Specific Strength
OHC	Open Hole Compression
OHT	Open Hole Tension
SRC	Stiffness Reduction Coefficient
TCFE	Transverse Compression Fracture Energy
TTFE	Transverse Tension Fracture Energy
UD	Uni-directional
UTS	Ultimate Tensile Strength
VCCT	Virtual Crack Closure Technique
WWFE	World-Wide Failure Exercise

Symbols

γ_{12}	In-plane Shear Strain
δ	Displacement
$\delta_{X,eq}^{0}$	Equavialent Displacement at Damage Initiation
$\delta_{X,eq}^{f}$	Equavialent Displacement at Complete Failure
Δt	Time Increment
ϵ_{ij}	Strain Tensor
η	Internal Friction
θ_{fp}	Angle of Fracture Plane
ν_{ij}	Poisson's Ratio

ρ	Density
σ_{ij}	Stress Tensor
τ	Shear Stress
C	Compliance
E	Modulus
d_f, d_m, d_s	Damage Variables for Fiber, Matrix, and Shear
df	Degradation Factor
E_{br}	Bearing Chord Stiffness
f_E	Stress Exposure Factor
FI	Failure Index
G_c	Fracture Energy
G_I, G_{II}	Strain Energy Release Rates for Mode I and Mode II
k_σ	Maximum Specific Strength
k_E	Maximum Specific Modulus
K	Interface Stiffness
l_{cz}	Cohesive Zone Length
$m_{\sigma f}$	Stress Magnification Effect
M	Damage Operator
P	Load
S	Allowable Shear Stress
t	Laminate Thickness
T	Step Time

X	Allowable Tensile or Compressive Stress

Superscripts and Subscripts

$1, 2, 3$	Longitudinal, Transverse, and Thickness Directions
T, C	Tension and Compression
f, m	Fiber and Matrix
L, T	Longitudinal and Transverse
br	Bearing

CHAPTER 1

INTRODUCTION

Composite materials consist of at least two different ingredients and offer material properties different from the constituent materials. The resultant material has some advantages to its constituents. In this study, some design issues for advanced composite structures used especially in the aerospace industry are considered. Fiber reinforced polymers (FRPs) have been highly popular for this area since weight is extremely important in air vehicles. In order to compare the mechanical performance of different materials; ultimate tensile stress (UTS), modulus, maximum specific strength (MSS) and maximum specific modulus (MSM) of different engineering materials and fibers which are used in FRPs are given in Table 1. As can be seen in the table, advanced fibers have significant advantages over conventional metals. With their high specific strength, composite materials allow to make light-weight air vehicles.

Table 1: Material properties [1]

Material	UTS, $[MPa]$	Modulus, $E\ [GPa]$	MSS, $k_\sigma x10^3\ [m]$	MSM, $k_E x10^3\ [m]$
Steel	400-2200	180-210	28.8	2750
Aluminum	140-700	69-72	26.5	2670
Titanium	420-1200	110	26.7	2440
Glass	3100-5000	72-95	200	3960
Carbon	7000	300	400	17100
Alumina (Al_2O_3)	2400-4100	470-530	100	13300

As Jones [2] stated, by using the full advantage of FRPs, more than 70% lighter structures can be obtained. Beside from weight advantages, in terms of design aspect, FRPs may offer better thermal and acoustic insulation, wear and corrosion resistance, fatigue life, and temperature-dependent behavior. Since 1960s, these advantageous make FRPs more attractive for airplanes. With developing design capabilities, percentage of composite structure use in airplanes has dramatically increased as seen in Figure 1.

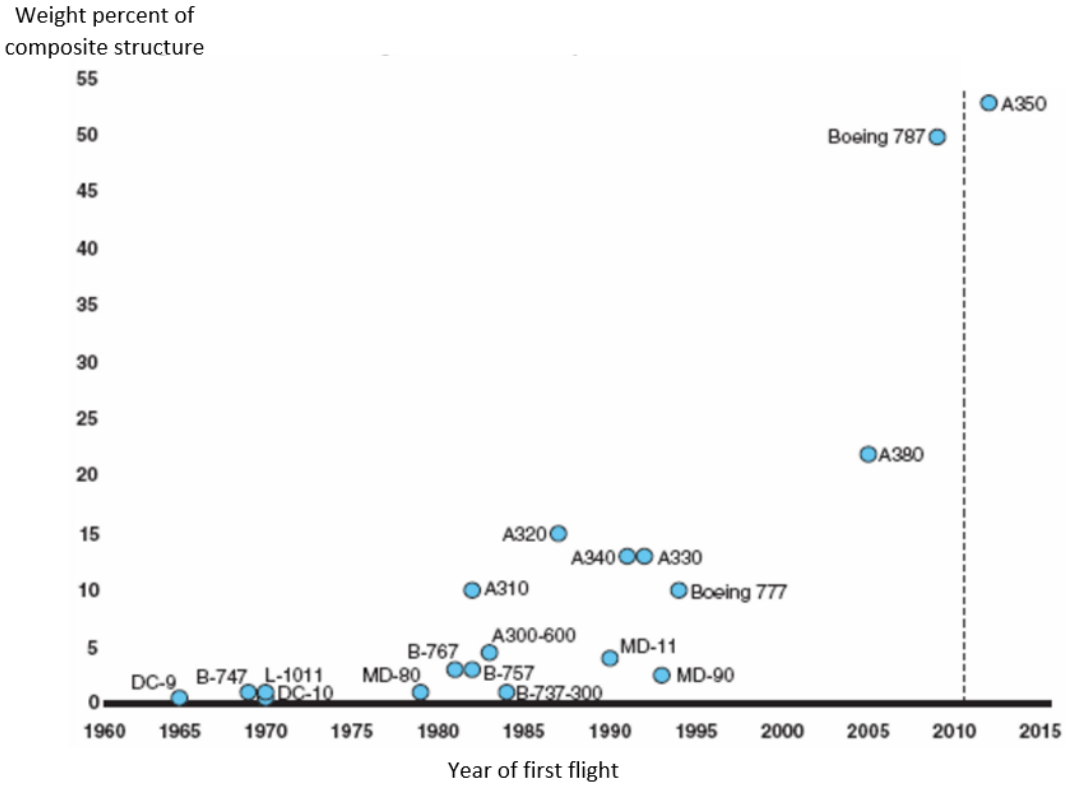

Figure 1: Weight percentage of composite structures on commercial airplanes [3]

Beside all these advantages, composite structures unfortunately have high manufacturing costs and there are still some limitations on design. High costs prevent FRPs to be used in other areas including the automotive industry. This problem may be overcome by benefiting from all advantageous of FRPs. This can be achieved for example by developing better design criteria. Having more reliable criteria reduces design and test costs and allows utilizing full advantage of light-weight structures.

Composite structures are also suitable for helicopter blades. They have high rotation speed so weight becomes crucial at these structures. Light-weight FRP blades are suitable for helicopters and have become more popular. Helicopter blades consists of various substructures like weight pocket, root, erosion shield which must be designed separately. The weight-pocket is especially considered in the scope of this thesis.

Weight-pockets are used to place balance weights on the blade. Considering the high rotor speed, helicopter blades must be well balanced to prevent unbalanced loads and to extend service life of the rotor. Its inertia causes a bearing load on the pocket surface. To simulate this case, a plate with hole is modelled and load is applied through a pin. Predicting ultimate load is important to reduce the test costs.

1.1 Scope of Thesis

In the scope of this thesis, a literature survey is conducted to present common failure criteria for composite structures. Since the composite structures have different failure mechanisms, it is essential to study previous work.

Further, methods to analyze composite structures are investigated. Progressive failure approach and cohesive zone method are explained and implemented in a numerical model. As a preparation for the model construction, a material characterization study is performed to obtain material properties of S2/Glass fiber and MTM49L matrix lamina which are needed for numerical model. This material characterization study is a part of SANTEZ project “Design Methodology for Thick Composite Laminates” which is supported by Ministry of Science, Industry and Technology, and Turkish Aerospace Industries (TAI).

Using the material characterization data, a numerical model is developed to simulate the weight pocket on helicopter blades. Progressive and sudden damage models are investigated. Cohesive layers are also added to the model to investigate delamination.

Finally, the specimens which simulate the weight pockets are tested. These test results are compared with numerical results.

1.2 Outline of Thesis

In this chapter, an introduction is presented and the scope of the thesis is explained step by step. In Chapter 2, failure of FRPs are explained under two parts; one is intra-laminar and the other is inter-laminar failure. Important failure criteria are explained by comparing predictive capabilities. Progressive failure method is also explained in this chapter. Material characterization tests are explained in Chapter 3 and material properties are given. In Chapter 4, numerical model which is developed to simulate weight-pocket is explained in detail, then results are presented and discussed by comparing with experimental data in Chapter 5. Finally in Chapter 6, a conclusion is given and planned future work are explained.

CHAPTER 2

LITERATURE SURVEY

Failure in composite structures are discussed mainly in two parts. The first part is the intra-laminar failure, which deals with the failure of plies themselves; and the latter is the inter-laminar failure or failure between layers.

Failure criteria which are developed to predict the intra-laminar failure is presented in this chapter in a chronological order. This type of failure approach considers only the failure of ply itself but does not deal with structural integrity.

Inter-laminar failure (delamination) is an important failure mode and must be included in the failure analysis. In this chapter, methods to include such effects is also discussed.

In addition to predicting the failure, the failure progression is also a critical design issue. Failure of a composite structure can be considered to be happening in a sudden manner or rather in many steps or a progressive manner. Basically, there are various approaches to predict failure progression. These methods are presented in the third section of this chapter.

2.1 Intra-Laminar Failure

Advanced composites, most commonly polymer matrix composites (PMCs), have been used in structures since 1960s. In terms of analysis of such structures, in those days the mechanics of monolithic materials was a developed area, so such analyses were applied to composite structures. However, they were not that successful since they are originally developed for metallic structures. As far as metals and composites

are concerned, there are clear differences in their corresponding failure mechanisms. Unlike metals, multiple failure types with completely different failure characteristics observed in composites. The term “criticality” indicates failure of composite to perform its design function [4].

In 1991, an expert meeting was organized by UK Science and Engineering Research Council and that was the origin of world-wide failure exercise (WWFE). The meeting called as ‘Failure of Polymeric Composites and Structures: Mechanisms and Criteria for the Prediction of Performance’ had two major outcomes. One conclusion was there was lack of faith in the failure criteria used in those days, and there was not any universal definition for failure. The second argument can be explained as the meaning of the word “failure” changes according to design expectations. For example; in case of a composite pipe, leakage can be considered as a design failure. On the other hand for a load carrying structure, a certain loss in stiffness can be very well taken as failure [5].

In WWFE meeting, failure prediction methods summarized in Table 1, and their prediction capabilities were examined. Findings in these approaches were compared with the experimental results [6].

Table 2: Failure Prediction Methods Examined in WWFE

Chamis	Eckold	Edge	Hart-Smith (1,2,3)	McCartney (A,B)
Puck	Rotem	Sun (L, NL)	Tsai (A, B)	Wolfe (A, B)
Zinoviev	Bogetti	Mayes	Cuntze (A, B)	Huang

NASA Langley Research Center examined the failure theories after WWFE, and introduced new approaches. LaRC03 and LaRC04 criteria were defined as a result of that study [7]. Nali and Carrera [7] classified failure theories under two main groups in terms of whether it is considering or neglecting interactions between stress components. For example, the maximum stress and the maximum strain criteria neglect interactions between stresses and strains, respectively. Authors also examined criteria with stress interactions under two groups. The Hoffman, Tsai-Wu, Liu-Tsai

and Tsai-Hill are introduced as failure criteria with a single inequality to define the failure envelope. However, in case of Hashin and Rotem, Hashin, Puck and Schuermann and LaRC03 criteria a combination of interactive and non-interactive conditions were proposed.

2.1.1 Maximum Stress Criterion

This approach considers stress components separately and assumes that the failure would occur when any of the stress components reach the allowable strength in a corresponding direction. This criterion proposes following inequalities to examine failure.

$$\sigma_{11} \geq X_1^T \ , \qquad \sigma_{11} \leq -X_1^C \ , \qquad \sigma_{22} \geq X_2^T \tag{1a}$$

$$\sigma_{22} \leq -X_2^C \ , \qquad \sigma_{12} \geq S \ , \qquad \sigma_{12} \leq -S \tag{1b}$$

Where *X* is the allowable stress and subscripts 1, 2 corresponds to fiber and transverse directions, while superscripts *T, C* stands for tension and compression, respectively; and *S* is the shear allowable. According to the criteria, if any of these inequalities is satisfied, the failure would occur. This failure envelop is graphically represented in Figure 2.

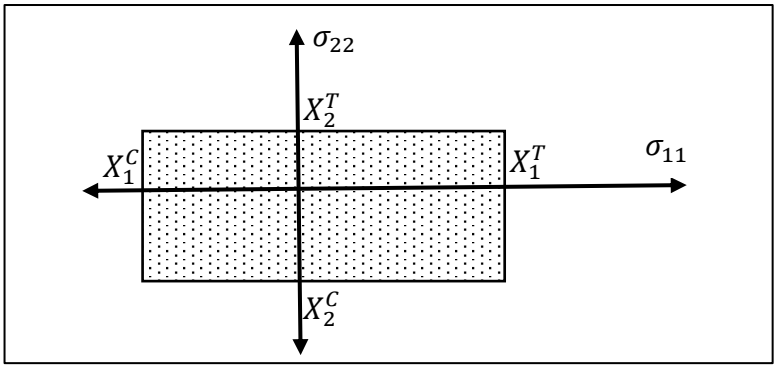

Figure 2: Maximum Stress Criterion

2.1.2 Maximum Strain Criterion

Similar to the maximum stress approach, allowable strains are utilized in this criterion. Failure criteria is given in terms of inequalities as follows:

$$\epsilon_{11} \geq e_1^T \ , \qquad \epsilon_{11} \leq -e_1^C \ , \qquad \epsilon_{22} \geq e_2^T \tag{2a}$$

$$\epsilon_{22} \leq -e_2^C \ , \qquad \epsilon_{12} \geq e_{12} \ , \qquad \epsilon_{12} \leq -e_{12} \tag{2b}$$

Where *e* is the allowable strain in the corresponding direction.

2.1.3 Tsai-Hill Criterion

In 1947, Hill [8] proposes a yielding criterion for anisotropic materials as follows:

$$F(\sigma_{yy} - \sigma_{zz})^2 + G(\sigma_{zz} - \sigma_{xx})^2 + H(\sigma_{xx} - \sigma_{yy})^2 + 2L\sigma_{yz}^2 + 2M\sigma_{zx}^2 + 2N\sigma_{xy}^2 = 1 \tag{3}$$

where *F, G, H, L, M, N* are constants representing the material anisotropy. They can be obtained with tests in the principal anisotropic directions. Also *x, y,* and *z* axes represent fiber, transverse, and normal directions, respectively.

After the failure criterion of Hill, Tsai [9] developed a theory for composite materials. For thin composites, he neglected out-of-plane stresses, i.e. $\sigma_3 = \tau_{13} = \tau_{23} = 0$. With this simplification Hill's failure criterion can be written as follows:

$$(G + H)\sigma_1^2 - 2H\sigma_1\sigma_2 + (H + F)\sigma_2^2 + 2N\tau_{12}^2 = 1 \tag{4}$$

Then, if the constants are replaced by material properties; *X, Y, Z* as normal strengths and *S* as shear strength:

$$\frac{1}{X^2}\sigma_1^2 - \left(\frac{1}{X^2} + \frac{1}{Y^2} - \frac{1}{Z^2}\right)\sigma_1\sigma_2 + \frac{1}{Y^2}\sigma_2^2 + \frac{1}{S^2}\tau_{12}^2 = 1 \tag{5}$$

Tsai also claimed that material properties are equal in the directions transverse to the fibers. So, *yz*-plane can be considered as isotropic. With these simplifications, failure criterion takes the following form:

$$\frac{1}{X^2}\sigma_1^2 - (\frac{1}{X^2})\sigma_1\sigma_2 + \frac{1}{Y^2}\sigma_2^2 + \frac{1}{S^2}\tau_{12}^2 = 1 \quad (6)$$

2.1.4 Tsai-Wu Criterion

Tsai and Wu, in 1971, proposed a modification for the previous anisotropic yield criterion. They suggested following equation [10]:

$$\begin{aligned} F_1\sigma_1 + F_2\sigma_2 + F_6\sigma_6 + F_{11}\sigma_1^2 + F_{22}\sigma_2^2 + F_{66}\sigma_6^2 \\ +2F_{12}\sigma_1\sigma_2 + 2F_{16}\sigma_1\sigma_6 + 2F_{26}\sigma_2\sigma_6 = 1 \end{aligned} \quad (7)$$

Then, they claimed that, sign change of the shear stress should be independent of material property; $F_{16} = F_{26} = F_6 = 0$.

Now, equation (7) can be simplified to:

$$F_1\sigma_1 + F_2\sigma_2 + F_{11}\sigma_1^2 + F_{22}\sigma_2^2 + F_{66}\sigma_6^2 + 2F_{12}\sigma_1\sigma_2 = 1 \quad (8)$$

F_1 and F_{11} are obtained by tensile and compressive tests in longitudinal direction; on the other hand, F_2 and F_{22} are obtained from tests in transverse direction. F_{66} can be obtained by calculating shear strength in shear test. As a result, constants in (8) are as follows:

$$F_1 = \frac{1}{X_1^T} - \frac{1}{X_1^C} \qquad F_{11} = \frac{1}{X_1^T X_1^C} \quad (9a)$$

$$F_2 = \frac{1}{X_2^T} - \frac{1}{X_2^C} \qquad F_{22} = \frac{1}{X_2^T X_2^C} \quad (9b)$$

$$F_{66} = \frac{1}{S^2} \quad (9c)$$

The remaining constant,F_{12}, must be evaluated by the biaxial test; however, it is a complicated test to conduct. As an alternative, Tsai and Hahn proposed that, $F_{12} = -0.5\sqrt{F_{11}F_{22}}$, can be used [10].

2.1.5 Hashin Criterion

In 1980, Hashin [11] made further studies on Tsai-Wu Criterion. He implies that Tsai-Wu Criterion had improvements over previous ones and it provided good fit with test data. However, Hashin also proposed that different failure modes can occur and a single quadratic function may not predict all of failure modes. On the other hand, proposing a failure criteria with higher than a quadratic degree would make things more complicated. As different from previous studies, Hashin examined fiber and matrix failure separately. By that way, instead of continuous failure surface a piece-wise continuous failure one is obtained [4].

In Hashin Criterion, σ_1 and σ_2 are not included for matrix and fiber failure, respectively. Since F_{12} term causes an uncertainty, this separate failure assumption solves this problem by not including the term.

For tensile fiber mode ($\sigma_{11} > 0$); Hashin [8] proposed following equation for the plane stress condition.

$$\left(\frac{\sigma_{11}}{X}\right)^2 + \left(\frac{\sigma_{12}}{T}\right)^2 = 1 \tag{10}$$

Or, using the maximum stress criterion:

$$\sigma_{11} = X \tag{11}$$

For the fiber compressive mode ($\sigma_{11} < 0$);

$$\sigma_{11} = X' \tag{12}$$

The matrix failure mechanism is more complicated. Hashin [8] introduced a failure plane whose normal makes an angle θ with y axis (transverse to the fiber direction). At this point Hashin examines the failure in two cases according to the normal stress, σ_{nn}, on the failure surface. Then, Hashin Failure Criterion takes the following forms for plane stress condition.

For the matrix tensile mode ($\sigma_{22} > 0$);

$$\left(\frac{\sigma_{22}}{Y}\right)^2 + \left(\frac{\sigma_{12}}{T}\right)^2 = 1 \tag{13}$$

For the matrix compressive mode ($\sigma_{22} < 0$);

$$\left(\frac{\sigma_{22}}{2T'}\right)^2 + \left[\left(\frac{Y'}{2T'}\right)^2 - 1\right]\frac{\sigma_{22}}{Y'} + \left(\frac{\sigma_{12}}{T}\right)^2 = 1 \tag{14}$$

2.1.6 Puck Criterion

In 2002, Puck and Schürmann [12] introduced a new study on the composite failure. Puck summarizes previous studies by pointing out important points. As mentioned in [9]; fiber failure and inter-fiber failure, which describes matrix failure, have totally different mechanisms; so, two independent failure criteria have to be applied. For transverse loading (σ_2), transverse compression and transverse tensile strength should be considered separately. After crack initiation, stiffness degradation should be gradual. As final remark, compressive and tensile crack formation should be distinguished for inter-fiber failure.

Fracture analysis of laminates is described in four steps [12]. First step, stress and strain analysis have to be implemented in ply-by-ply basis. As the second step, fracture criteria have to be applied for plies. As the third, a degradation model have to be applied. Finally, an iteration is needed to follow these steps to simulate gradual fracture.

Puck and Schürmann [12], mentioned the non-linear relationship between stress and strain especially in ($\sigma_{21}, \epsilon_{21}$) and ($\sigma_2, \epsilon_2$) which is not included in classical laminate theory. This non-linear relation is presented in Figure 3.

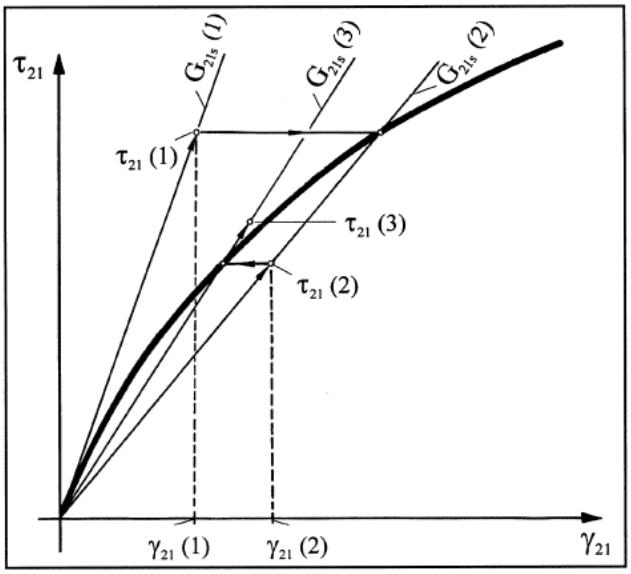

Figure 3: Non-linear Relation between Stress and Strain [12]

Another point emphasized by Puck et al. [12] is that the stress-strain diagrams change with the existence of other stresses. This condition can be observed in Figure 4.

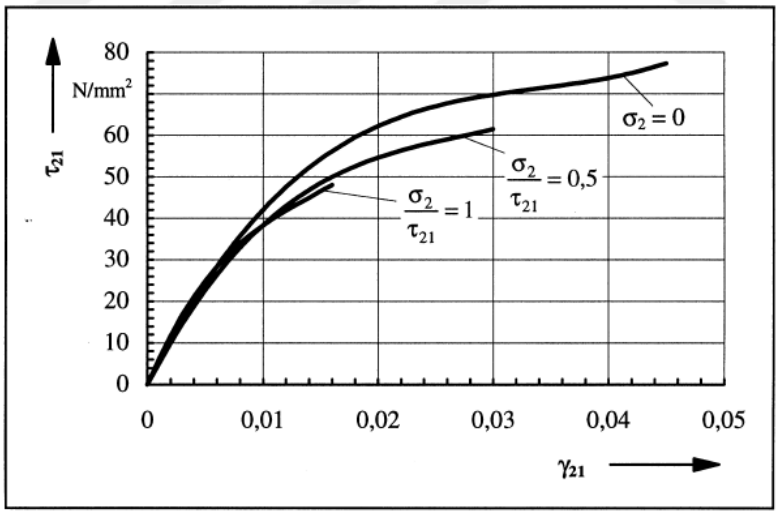

Figure 4: Effect of Combined Loading on Stress-Strain Relation [12]

As different from previous discussions, Puck and Schürmann [12] analyses stress and strain as different on fibers and matrix, instead of considering whole laminate. For this approach, 'stress magnification effect' ($m_{\sigma f}$) is introduced. Since the elastic moduli

of matrix and fiber are different, transverse loading causes different stress on fiber and matrix. These approaches lead to the following conditions for fiber failure.

$$\frac{1}{\epsilon_{1T}}\left(\epsilon_1 + \frac{\nu_{f12}}{E_{f1}} m_{\sigma f}\sigma_2\right) = 1 \quad \text{for tension} \tag{15a}$$

$$\frac{1}{\epsilon_{1C}}\left(\epsilon_1 + \frac{\nu_{f12}}{E_{f1}} m_{\sigma f}\sigma_2\right) = -1 \quad \text{for compression} \tag{15b}$$

where the subscripts 'f' stand for fiber, and $\epsilon_{1T}, \epsilon_{1C}$ are allowable strains for tension and compression.

Similar to Hashin Criterion, Puck Failure Criterion also defines a failure plane for inter-fiber failure [12]. This failure mechanism is schematically presented in Figure 5.

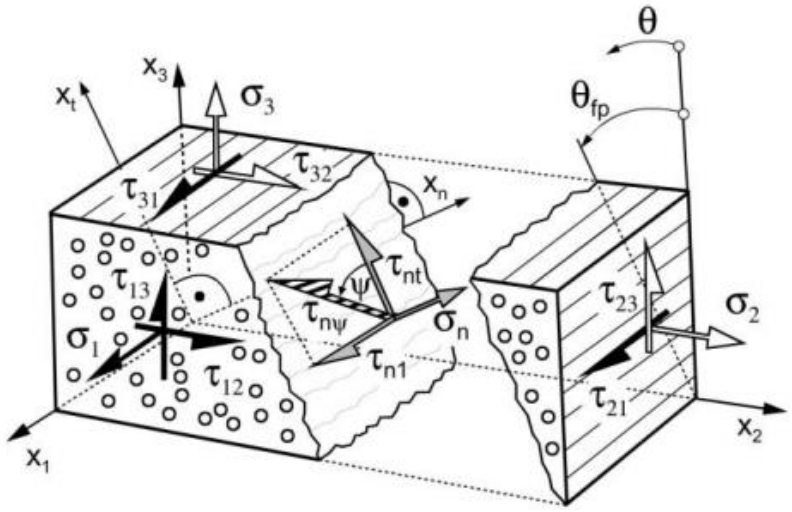

Figure 5: Failure Plane for Inter-Fiber Failure [13]

Here, failure for inter-fiber is separated into three modes. For Mode *A*, tensile transverse stress ($\sigma_2 \geq 0$) and shear stress (σ_{21}) are applied and angle of fracture plane is taken as zero ($\theta_{fp} = 0$). Mode *B* is similar with Mode *A*, but the transverse stress is compressive ($\sigma_2 \leq 0$). For Mode *C*, applied stresses are same with Mode *B*, but compressive stress is more dominant. This difference results in different failure

mechanism with 45° failure planes. The fracture curve which describes these modes is given in Figure 6.

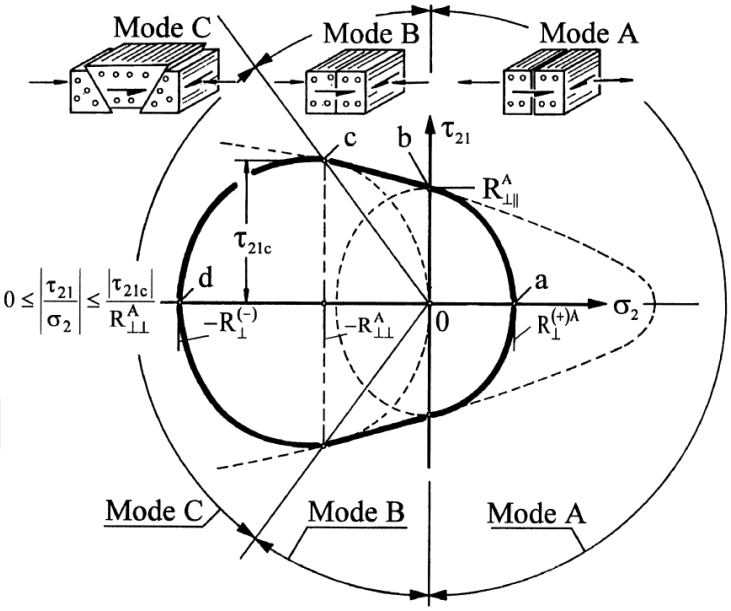

Figure 6: Inter-Fiber Failure Mechanism

For this failure criterion, determining inclination angel of failure plane becomes important to predict fracture. Puck et al. [13] define a stress exposure factor, $f_E(\theta)$. This angle dependent factor defines 'risk of fracture' for any stress plane with an inclination of angle θ. Then, fracture plane can be found by calculating the inclination angle which makes the exposure factor, $f_E(\theta)$, maximum.

2.1.7 LaRC03 Criterion

After the evaluations in WWFE, in 2005 Davila et al. started new discussions on Hashin's and Puck's criteria [14] which is named as LaRC03. LaRC03 is based on Hashin's failure model and Puck's failure plane concept for the matrix compression. This phenomenological approach solves the angle of failure plane by maximizing the Mohr-Coulomb effective stresses. Their work also deals with fiber misalignment and

suggests a criterion for fiber kinking for fiber compression. For matrix tension LaRC03 is also including in-situ strength concept; which can be explained as adjacent plies with different orientation angles have a constraining effect, so effective stress of a ply should be increased.

For determining angle of fracture plane, Davila et al. [14] proposed a matrix failure index (FI_M) for the transverse compression case. The matrix failure index is

$$FI_M = \left(\frac{\tau_{eff}^T}{S^T}\right)^2 + \left(\frac{\tau_{eff}^L}{S_{is}^L}\right)^2 \leq 1 \tag{16}$$

where subscript "*eff"* means effective stress and superscripts *T* and *L* stands for transverse and longitudinal stresses, respectively. So, the fracture plane is expected to have an angle which makes the matrix failure index maximum. In Figure 7, angle of fracture for different load combinations is given.

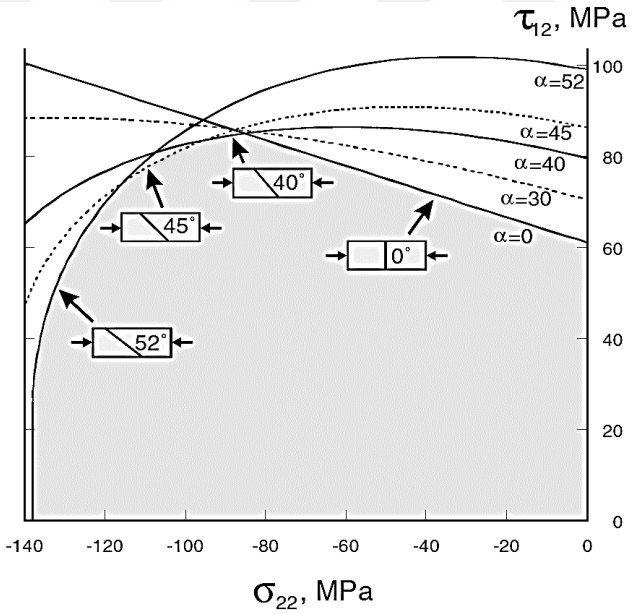

Figure 7: Matrix Failure Envelopes for UD E-Glass-Epoxy Lamina [14]

For the case of transverse tension and in-plane shear stresses, Davila et al. [14] have the following failure index model, which is a modified form of Hashin Criterion with in-situ strengths included.

$$FI_M = (1-g)\frac{\sigma_{22}}{Y_{is}^T} + g\left(\frac{\sigma_{22}}{Y_{is}^T}\right)^2 + \left(\frac{\tau_{12}}{S_{is}^L}\right)^2 \leq 1 \tag{17}$$

Davila et al. [14] choose to use the maximum strain criterion for the fiber tension failure since it is simple to measure. But the fiber compression is more complicated than tension, since failure under the fiber compression can be formed in two ways. Failure criterion for fiber kinking is

$$FI_F = \langle \frac{|\tau_{12}^m| + \eta^L \sigma_{22}^m}{S_{is}^L} \rangle \leq 1 \tag{18}$$

where η is the internal friction coefficient and superscript *'m'* means matrix. Finally, the criterion for the matrix tension under the fiber compression is

$$FI_F = (1-g)\left(\frac{\sigma_{22}^m}{Y_{is}^T}\right) + g\left(\frac{\sigma_{22}^m}{Y_{is}^T}\right)^2 + \left(\frac{\tau_{12}^m}{S_{is}^L}\right)^2 \leq 1 \tag{19}$$

In Figure 8, common failure criteria are compared with WWFE test data.

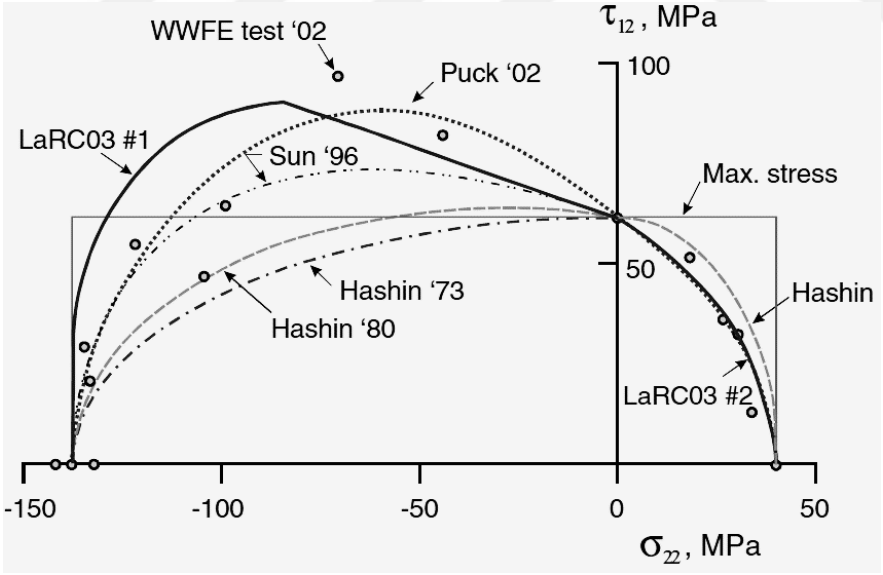

Figure 8: Failure Envelopes for UD E-Glass/LY556 [14]

2.1.8 LaRC04 Criterion

After LaRC03, Pinho et al. [15] suggest a new criterion by extending LaRC03 for three dimensional (3D) loading and in-plane shear non-linearity. In LaRC04, the matrix compression is considered as modified 3D Puck criterion. For the matrix compression, Mohr-Coulomb model is used for fracture angle prediction. LaRC04 model predicts the fiber kinking plane and presents six equations for design as follows:

Matrix Tensile Failure ($\sigma_{22} \geq 0$):

$$FI_M = (1-g)\frac{\sigma_2}{Y_{is}^T} + g\left(\frac{\sigma_2}{Y_{is}^T}\right)^2 + \frac{\Lambda_{23}^o \tau_{23}^2 + \chi(\gamma_{12})}{\chi(\gamma_{12,is}^u)} \tag{20}$$

Matrix Compressive Failure ($\sigma_{22} < 0$):

$$FI_M = \left(\frac{\tau^{Tm}}{S^T - \eta^T \sigma_n^m}\right)^2 + \left(\frac{\tau^{Lm}}{S_{is}^L - \eta^L \sigma_n^m}\right)^2 \quad \text{for } \sigma_{11} < -Y^C \tag{21a}$$

$$FI_M = \left(\frac{\tau^{T}}{S^T - \eta^L \sigma_n}\right)^2 + \left(\frac{\tau^{L}}{S_{is}^L - \eta^L \sigma_n}\right)^2 \quad \text{for } \sigma_{11} \geq -Y^C \tag{221b}$$

Fiber Tensile Failure ($\sigma_{11} \geq 0$):

$$FI_F = \frac{\sigma_{11}}{X^T} \tag{22}$$

Fiber Tensile Failure ($\sigma_{11} \geq 0$):

$$FI_F = \left(\frac{\tau_{1^m 2^m}}{S_{is}^L - \eta^L \sigma_{2^m 2^m}}\right)^2 \quad \text{for } \sigma_{2^m 2^m} < 0 \tag{233a}$$

$$FI_{M/F} = (1-g)\frac{\sigma_{2^m 2^m}}{Y_{is}^T} + g\left(\frac{\sigma_{2^m 2^m}}{Y_{is}^T}\right)^2 + \frac{\Lambda_{23}^o \tau_{2^m 3^\psi}^2 + \chi(\gamma_{1^m 2^m})}{\chi(\gamma_{12,is}^u)} \quad \text{for } \sigma_{2^m 2^m} \geq 0 \tag{23b}$$

Where; Λ = Crack tensor - $\Lambda_{23}^o = 2(\frac{1}{E_{22}} - \frac{\nu_{21}^2}{E_{11}})$

$$\chi(\gamma_{12}) = 2\int_0^{\gamma_{12}} \tau_{12} d\gamma_{12}$$

Kinking geometry and stress components are presented in Figure 9.

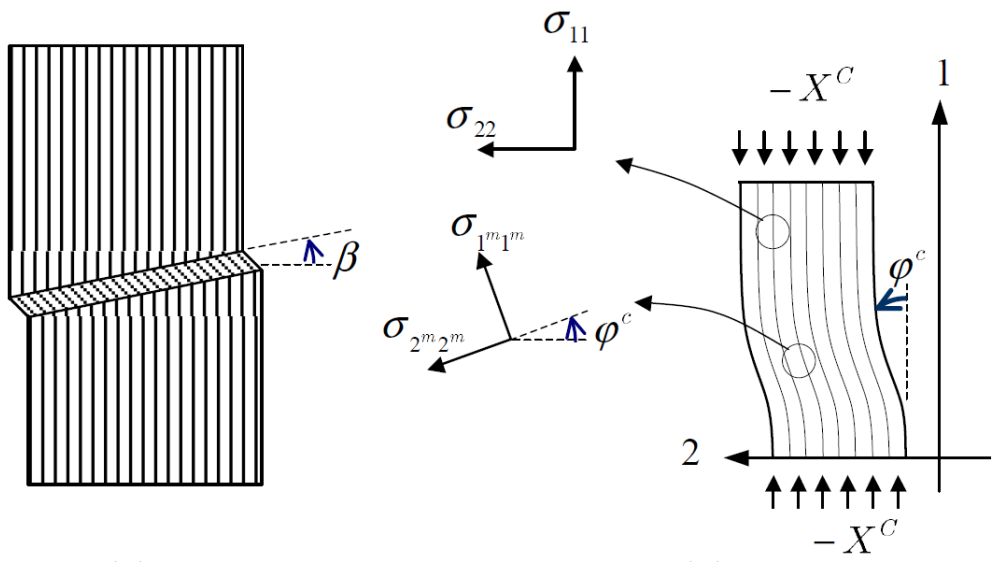

Figure 9: Kinking geometry and stress components [15]

In this chapter, important failure criteria for FRPs are discussed in chronological order. Failure analysis starts with the application of anisotropic yield criteria which is valid for metals to composites. Since the anisotropic yield function is not practical, Hill [8] proposes a criterion by assuming plane stress and *YZ* plane as isotropic. Tsai and Wu [10] suggest that sign of the shear term is independent of material property, so that three constants in yield equation is eliminated. They also make an approximation for F_{12} term, which is difficult to determine. After that, Hashin [11] discusses that there is not a single failure mechanism for FRPs, so single quadratic equation cannot estimate failure for all modes. Then, he examines the failure separately for fiber and matrix. However, stress interactions still are not included for failure analysis and there is not any criterion for inter-laminar failure. Puck et al. [12] develop Hashin Criterion by introducing a fracture plane for transverse compression loads. In WWFE [16], Puck Criterion is introduced as one of the best criteria with good predictive capabilities. LaRC03 [14] is an improved version of Puck Criterion, which makes suggestions on calculation of fracture plane. This criterion also includes the in-situ strength concept

to the analysis. LaRC03 is modified as including 3D stress states and non-linarites and introduced as LaRC04 by Pinho et al. [15].

In Figure 10, comparison of failure criteria and experimental results for transverse and shear loading is presented. As seen from the graph, for tensile loading conditions all methods give close results. On the other hand, for transverse compressive stress, improvement of failure criteria can be seen. For this case, Hashin gives conservative results. As expected Puck has better predictive capability than Hashin. As mentioned before, LaRC04 is a modified version of Puck criterion and main difference is including 3D stress states; so, they result in very close failure envelopes.

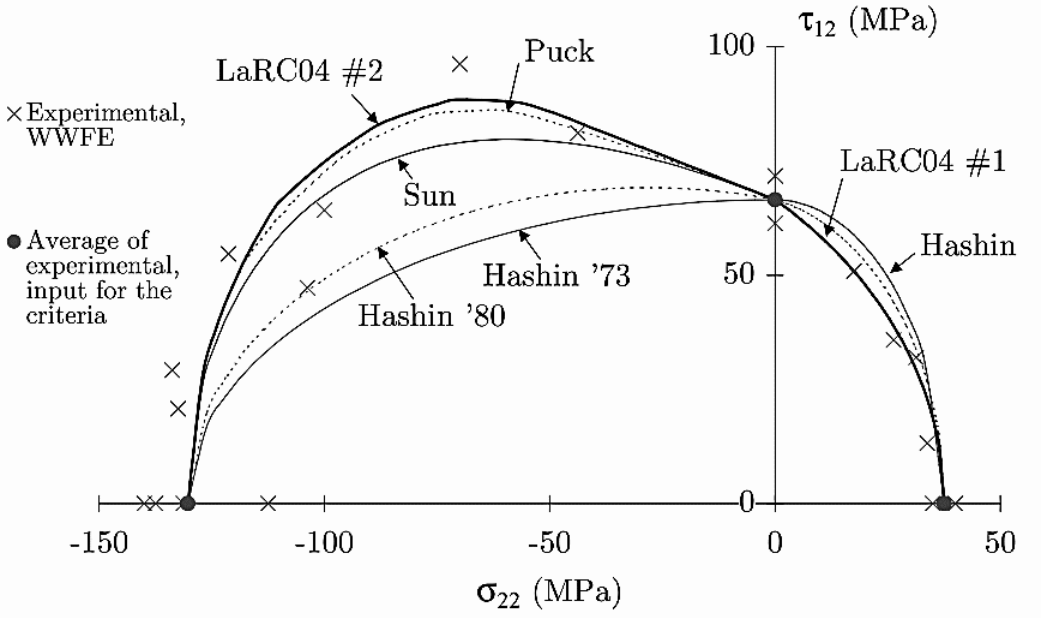

Figure 10: Comparison of Failure Criteria [15]

2.2 Inter-Laminar Failure

Inter-laminar damage (delamination) is an important concept for laminated composite structures. Delamination can be caused from manufacturing defect or impact. If there is not any reinforcement in thickness direction, delamination may trigger intra-laminar failure and cause local degradation of properties [17]. However, failure criteria

discussions up to this point do not consider delamination in their predictions. So, different methods are developed for delamination analysis. The virtual crack closure (VCCT), the J-integral, the stiffness derivative techniques are examples for that methods [18].

Krueger [19], summarizes VCCT as the approach which assumes the fracture energy to extend the crack with an amount of Δa is equal to the required energy to close the crack with the same amount (Figure 11). It is proposed that, energy released, ΔE, for crack extension from $a + \Delta a$ to $a + 2\Delta a$ is equal to energy required to close the crack betwen nodes i and k.

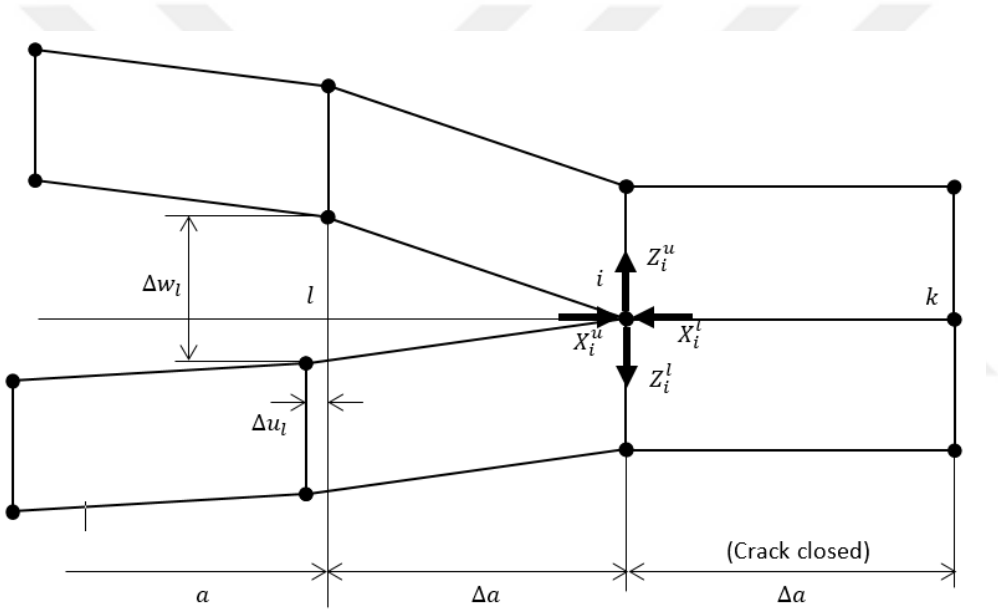

Figure 11: VCCT geometry [19]

On the other hand, Yang and Cox [20] point out the drawbacks of VCCT. Instability at the crack tip, requirement for an initial crack, assumption of the crack tip does not change shape (which is not the case generally), and small element size requirement at the crack tip are the ones which are emphasized by the authors.

The J-integral method, which is proposed by [21], suggests a line integral that surrounds the strain concentration region around the crack tip. The method is geometrically presented in Figure 12.

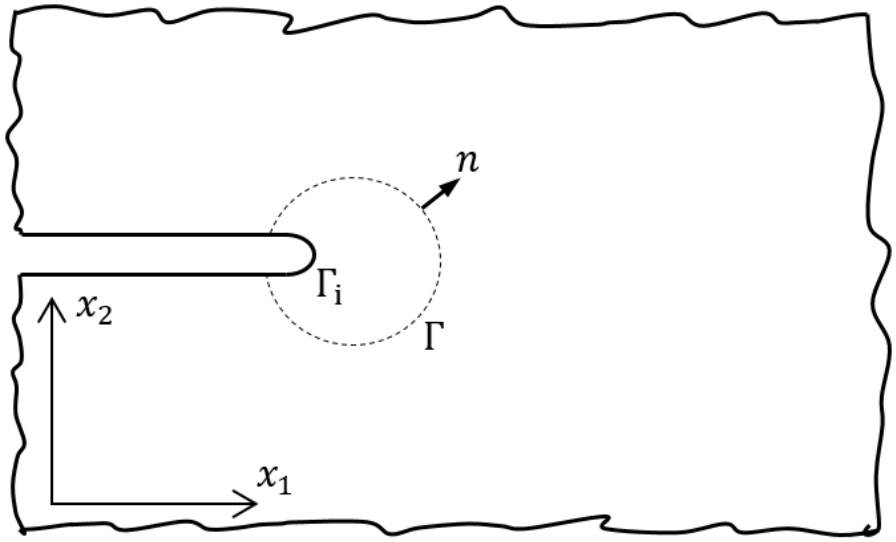

Figure 12: The J-integral method [21]

In 1974, Parks [22] proposes stiffness derivative finite element method which is a modified version of J-integral. The method uses the energy release rate, and does not require any special element or a second solution for small changes in crack length. Parks confirms the method for 2D problems but not suitable for 3D modeling.

Another approach to predict delamination is using decohesion finite elements. Decohesion finite elements can be used by Cohesive Zone Model (CZM) approach. This model is used by implementing artificial decohesion layers between composite ones, and the crack propagation is modeled in these layers. CZM properties are determined according to bulk material, crack initiation condition and crack evaluation function [23].

Turon et al. [23], emphasize two condition for an appropriate CZM. First, in order to avoid from an artificial compliance, the cohesive compliance should be small; and second, element size in the FEM should be smaller than cohesive zone length.

For the stiffness of interface, K, is determined by following equation [24]:

$$K = \frac{\alpha E_3}{t} \tag{24}$$

where α is a parameter which is suggested as greater than 50, to accomplish loss of stiffness less than 2% [24] and t is the thickness of sub-laminate. Implementation of cohesive layer is presented in Figure 13.

Figure 13: Implementation of cohesive layer

2.3 Progressive Failure Method

Failure concept for composite materials is complicated than conventional materials. Failure is defined as losing its functionality previously. So, there is not any general failure definition for composites. For some cases first ply failure (FPF) can be considered as failure, but this approach is conservative in general. According to OHT test results, given in Figure 14, first ply failure is observed around 20 kN; however, final failure is observed around 48 kN.

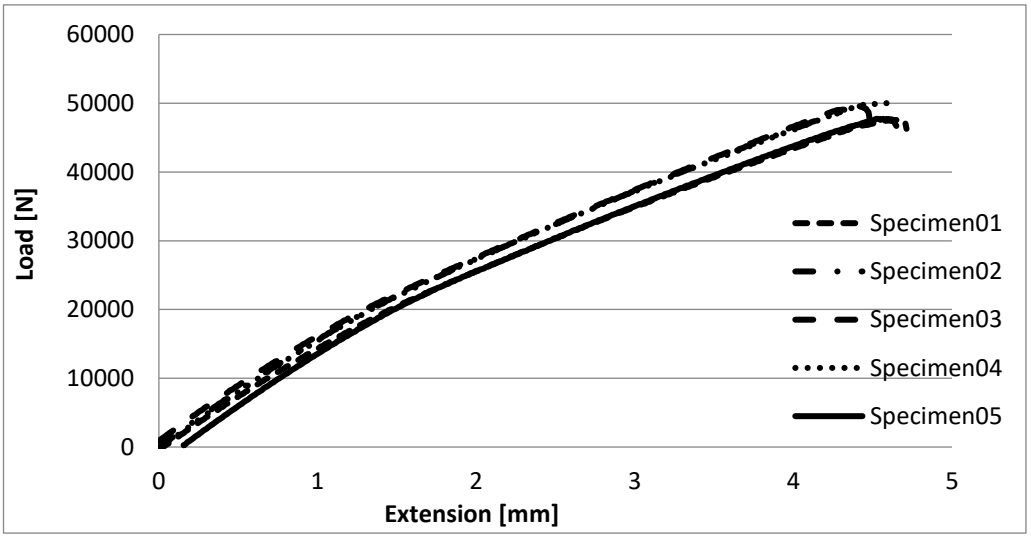

Figure 14: OHT Load-Extension plot

Tsai [25] in his book, implies that in order to analyze further load-carrying capability of the laminate under non-homogeneous stresses, an iterative degradation model must be applied for plies after FPF. On the other hand, for homogeneous stress cases, simultaneous failure should be preferred for simplicity.

Liu and Tsai [26], explain the procedure for progressive failure as a part of WWFE. After FPF, the transverse strain on the failed ply is important. Only if, there is a positive transverse strain, micro-cracking occur, and matrix modulus is reduced. On the other hand, fiber failure is the only possible mode, if the transverse strain is zero or compressive. Fiber failure is named as catastrophic failure; so, matrix failure cannot be applied after that. This ply-by-ply degradation method continue until ultimate load.

Matzenmiller and Taylor [27] implies that, micro-crack formation in matrix which is generally caused by transverse or shear loading causes stiffness degradation. On the other hand, permanent deformations are very small; so, assuming that element or ply as totally failed is not logical; since, it still carries load. There are failure criteria which predict failure onset for different damage mechanisms, but they are insufficient to predict final failure under the condition of failure progression (Maimi et al., 2007) [28].

A failure progression analysis generally follows the following steps. The first step is to establish equilibrium by using a non-linear analysis. Secondly, the lamina stress state is determined. Thirdly, failure is checked by a failure criterion and the corresponding failure mode is determined. As the fourth step, a material degradation model should be applied and material properties are modified according to this model. Finally, equilibrium is re-established and this procedure continue until the final failure of the structure (Sleight, 1999) [29]. In Figure 15, flowchart of Sleight model [29] is presented.

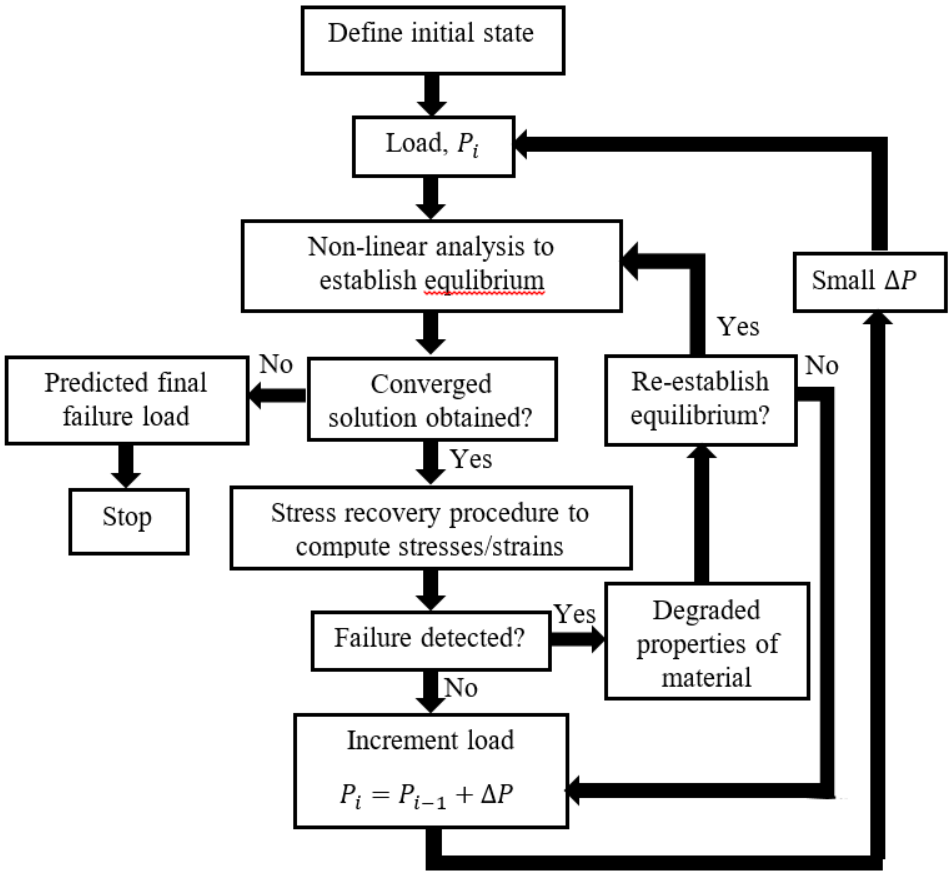

Figure 15: Progressive failure flowchart [29]

After the progressive failure model is decided, a degradation model is required. Here, the degradation can either be implemented by instantaneously reducing material

properties, or a gradual degradation model can be used [30]. Garnich and Akula [30] examine and compare degradation models in their article.

There is the model Reddy and Reddy [31]. They suggest two models which are named as independent and interactive. For the independent model, it is claimed that each stress eventually causes degradation in the corresponding property only. On the other hand, for the interactive model, shear and normal properties are also affected. In the independent model, the stress to strength ratios for six stress components are compared and the maximum one is determined. After determining the critical stress by such analysis, a degradation is applied to the corresponding property. For the interactive model, the critical stress component is determined by calculating a failure index. Depending on the maximum index, failure is categorized as fiber failure (FF), matrix failure (MF) and/or delamination (DL). They use a "stiffness reduction coefficient" (SRC) for the sudden degradation. Their model is summarized in Table 3 and letter *R* indicates SRC.

Table 3: Reddy and Reddy degradation model [30]

Stress	E_{11}	E_{22}	E_{33}	G_{23}	G_{13}	G_{12}	ν_{12}	ν_{23}	ν_{13}	ν_{21}	ν_{31}	ν_{32}
	Non-interactive Model											
σ_{11}	R	-	-	-	-	-	R	-	R	-	-	-
σ_{22}	-	R	-	-	-	-	-	R	-	R	-	-
σ_{33}	-	-	R	-	-	-	-	-	-	-	R	R
σ_{23}	-	-	-	R	-	-	-	-	-	-	-	-
σ_{13}	-	-	-	-	R	-	-	-	-	-	-	-
σ_{12}	-	-	-	-	-	R	-	-	-	-	-	-
	Interactive Model											
FF	R	-	-	-	R	R	R	-	R	-	-	-
MF	-	R	-	R	-	R	-	R	-	R	-	-
DL	-	-	R	R	R	-	-	-	-	-	R	R

In some models, the fiber failure is considered as catastrophic and all material properties should be degraded for such cases. For example, Lee's model which is explained by Garnich et al. [30], considers three failure modes; FF, MF, DL. As seen in Table 4, Lee degrades all properties for FF.

Table 4: Lee model [30]

FM	C_{11}	C_{12}	C_{13}	C_{22}	C_{23}	C_{33}	C_{44}	C_{55}	C_{66}
FF	0	0	0	0	0	0	0	0	0
MF	-	0	-	0	0	-	0	-	0
DL	-	-	0	-	0	0	0	0	-

Another model which is implied in an article [30] is Hwang and Sun's model. For failure prediction they use the average integration point stresses. They propose that the complete failure occurs when matrix and fiber failure are observed at the same time. In case of delamination, their model proposes remodeling of the finite element model by defining delamination as a free surface. Their model is summarized in Table 5.

Table 5: Hwang and Sun model [30]

FM	C_{11}	C_{12}	C_{13}	C_{22}	C_{23}	C_{33}	C_{44}	C_{55}	C_{66}
FF	0	0	0	-	-	-	-	0	0
MF	-	0	-	0	0	-	0	-	0
FF + MF	0	0	0	0	0	0	0	0	0

Garnich and Akula [30] define the gradual degradation as the model at least one property is degraded with a function of evolving field variable. E^d is defined as the degraded property, while E is the undamaged property. These two parameters are related with a degradation factor, df, which is given as follow:

$$df = \frac{E^d}{E}, \quad 0 \leq df < 1 \tag{25}$$

The gradual degradation is presented in Figure 16, where path OBCD represents the sudden degradation; on the other hand, path OBD shows the gradual degradation. Function of BD is dependent on the model [30].

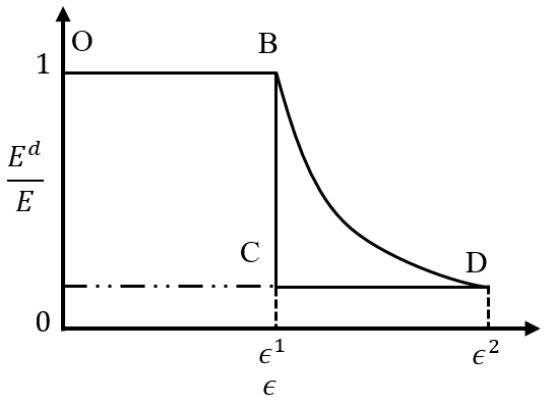

Figure 16: Degradation model [30]

Another degradation approach is named as ‘damaged tensor based model’ [30]. For this model a damage parameter which is expressed in terms of the degradation factor, df, is introduced. The degradation factor is unity for undamaged material and zero for the complete damage. So, a material property degrades to zero for the complete damage as shown in following equations.

$$D = f(1 - df) \tag{26}$$

$$E^d = E(1 - D) \tag{27}$$

For this type of degradation Lapczyk and Hurtado [32] use Matzenmiller [27] model. The effective stress, σ_{eff}, is defined as follows,

$$\sigma_{eff} = \boldsymbol{M}\sigma \tag{28}$$

where $\boldsymbol{M}$ is the damage operator, and given as follows,

$$\boldsymbol{M} = \begin{bmatrix} \frac{1}{1-d_f} & 0 & 0 \\ 0 & \frac{1}{1-d_m} & 0 \\ 0 & 0 & \frac{1}{1-d_s} \end{bmatrix} \tag{29}$$

d_f, d_m, d_s are damage variables for fiber, matrix and shear failure modes, respectively.

Then, by including Poisson's ratio degradation and using a damage operator, the damage compliance and stiffness matrices are given as follow;

$$\boldsymbol{H} = \begin{bmatrix} \frac{1}{(1-d_f)E_1} & -\frac{\nu_{21}}{E_2} & 0 \\ -\frac{\nu_{12}}{E_1} & \frac{1}{(1-d_m)E_2} & 0 \\ 0 & 0 & \frac{1}{(1-d_s)G_{12}} \end{bmatrix} \tag{30}$$

$$\boldsymbol{C} = \frac{1}{D}\begin{bmatrix} (1-d_f)E_1 & (1-d_f)(1-d_m)\nu_{21}E_1 & 0 \\ (1-d_f)(1-d_m)\nu_{12}E_2 & (1-d_m)E_2 & 0 \\ 0 & 0 & D(1-d_s)G_{12} \end{bmatrix} \tag{31}$$

where $D = 1 - (1-d_f)(1-d_m)\nu_{12}\nu_{21}$ and $E_1, E_2, G_{12}, \nu_{12}, \nu_{21}$ are undamaged material properties. The damage variable is assumed as follows;

$$d_X = \frac{\delta_{X,eq}^f(\delta_{X,eq} - \delta_{X,eq}^0)}{\delta_{X,eq}(\delta_{X,eq}^f - \delta_{X,eq}^0)}; \quad \delta_{X,eq}^0 \le \delta_{X,eq} \le \delta_{X,eq}^f \tag{32}$$

Since all damage variables have the same definition, X stands for ft, fc, mt, mc; where f and m denotes fiber and matrix, and t and c are for tensile and compressive, respectively. On the other hand, $\delta_{X,eq}^0$ is the equavialent displacement at damage initiation and $\delta_{X,eq}^f$ is the equavialent displacement at complete failure and can be determined with following equation,

$$\delta_{X,eq}^{f} = \frac{2G_{X,c}}{\sigma_{X,eq}^{0}} \tag{33}$$

This method requires to determine the fracture energies for each mode which can be seen in Figure 17.

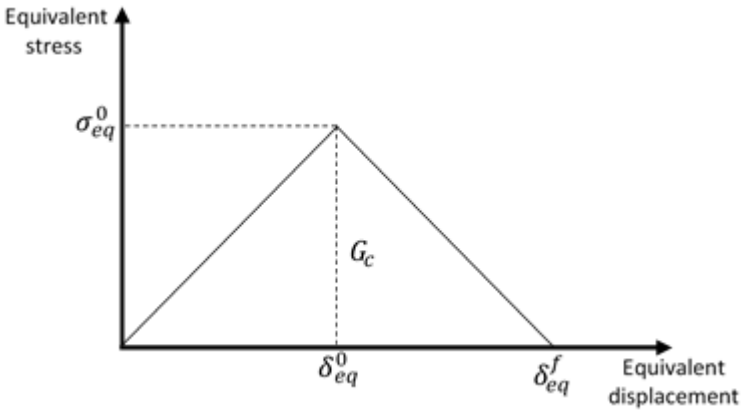

Figure 17: Equivalent stress versus equivalent displacement [33]

The fracture energy for matrix tension, $G_{mt,c}$ is known as Mode-I fracture toughness and can be determined by the double cantilever beam (DCB) test [34]. Maimi et al. [34] propose an equation for the fracture energy in case of matrix compression. For the matrix compression fracture energy, Mode-II fracture toughness is required which can be determined by the end notched flexure (ENF) test.

$$G_{mc,c} = \frac{G_{II}}{\cos\alpha_0} + at\mu Y_c \cos\alpha_0 \tag{34}$$

where $\alpha = 53° \pm 3°$ and t is the lamina thickness. a is a parameter between 0 and 1, 0 for the unidirectional laminate and 1 for a strongly confined lamina [34]. For the fiber tensile fracture energy, Pinho [35] proposed he compact tension (CT) test method. Bazant et al. [36] suggest the following approximation for the energy dissipated in a kink band:

$$G_{fc,c} = \frac{w}{s} G_{II} \tag{35}$$

where *w* is the kink band width and *s* is the distance between two matrix cracks. These variables are given in Figure 18.

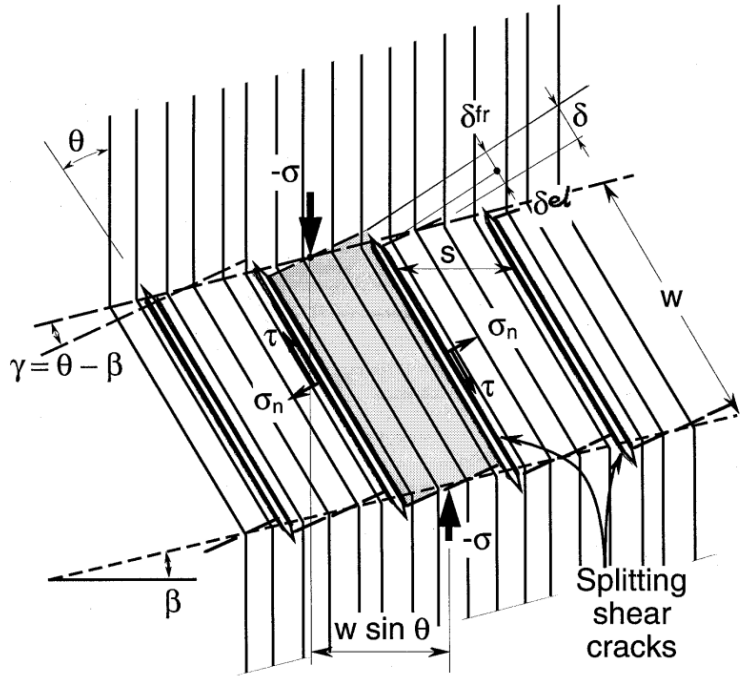

Figure 18: Kink band geometry [36]

A model with the gradual degradation according to the fracture toughness is used by Abaqus® for the progressive failure analysis of fiber reinforced composite materials [33].

To conclude, the implementation of the progressive failure method to failure analysis is very important when the nature of the FRPs considered. As shown in Figure 14, FPF and FF are observed at very different loads. So, considering a minor failure in one mode, as the final failure criterion is not logical.

Then, to consider progressive failure, sudden degradation models are easy to implement and requires a damage initiation criteria only. However, when the nature of the damage progression is considered sudden degradation may not predict the ultimate failure. Gradual degradation is more logical but determination of degradation parameters is difficult and model can be too complicated. An energy based degradation approach is seem to be the best one; since, it considers the amount of energy which is

needed to reach the complete failure. Only assumption in this approach is the path of failure after the damage initiation. Main drawback of energy based models is that determination of fracture energy is difficult.

CHAPTER 3

MATERIAL CHARACTERIZATION

Fiber Reinforced Plastics (FRP) are the most attractive materials especially in aerospace, automotive and railway industries due to their light-weight and high strength. On the other hand, the material property library for FRPs is limited unlike metals. So, the material characterization is a crucial step to obtain reliable results in analyses. The material characterization consists of a test series which can be grouped as coupon tests and fracture toughness tests. Coupon tests are conducted to determine material properties including but not limited to stiffness, ultimate tensile strength (UTS), ultimate tensile strain for compression and tension, Poisson's ratio, shear modulus and shear strength, the effect of holes and bearing characteristics. On the other hand, fracture toughness tests are needed to determine the energy release rate of material. Double cantilever beam (DCB) and end notched flexure (ENF) tests are performed for Mode-I and Mode-II cases, respectively. With these tests, after initiation, the crack propagation can be observed under tensile and shear loading. Energy release rates are required for the delamination analysis. The test program as a part of this study is performed in Solid Mechanics Laboratory of Mechanical Engineering, METU.

3.1 Coupon Tests

Coupon tests are the one of the way of determining mechanical properties of materials. Depending on the material and required property, there are different test standards. These standards specify test conditions, specimen types and geometries, test

procedures, calculation methods. In this study, coupon tests are performed with Instron® 1255 test machine which has 250 kN static load capacity. The displacement control condition is chosen for tests and test speed is arranged according to the corresponding standard. Strain gages are used for strain measurement during tension tests. A Dewesoft® data acquisition device provide communication between gages and Instron® control unit.

Ultimate tensile strain, UTS, Poisson's ratio and modulus are determined for the longitudinal and transverse directions with tension tests. Since FRPs behave differently in tension and compression, the compression tests are conducted for ultimate compressive stress and modulus in compression. Another required property, the shear modulus is determined by in-plane shear tests. Lastly, open hole tension (OHT) and open hole compression (OHC) tests are performed to investigate the effect of a hole.

3.1.1 Tension Test

Two sets of tension tests are performed; one is longitudinal in which load is applied to the unidirectional specimen in fiber direction, and the other one is in the transverse direction, which is perpendicular to the fiber direction. Ultimate tensile strength, ultimate tensile strain, Poisson's ratio and modulus of materials. Tests and calculations are conducted according to ASTM D3039 Standard [37]

Three strain gages are mounted on specimens, two in tension direction to increase accuracy and another one in the transverse direction is used to determine Poisson's ratio. Strain gages are essential to obtain the local strain data. Specimens are grapped by the test machine from tabs which are bonded to the composite specimen to prevent crushing due to the grips. A transverse glass specimen with strain gages is shown in Figure 19.

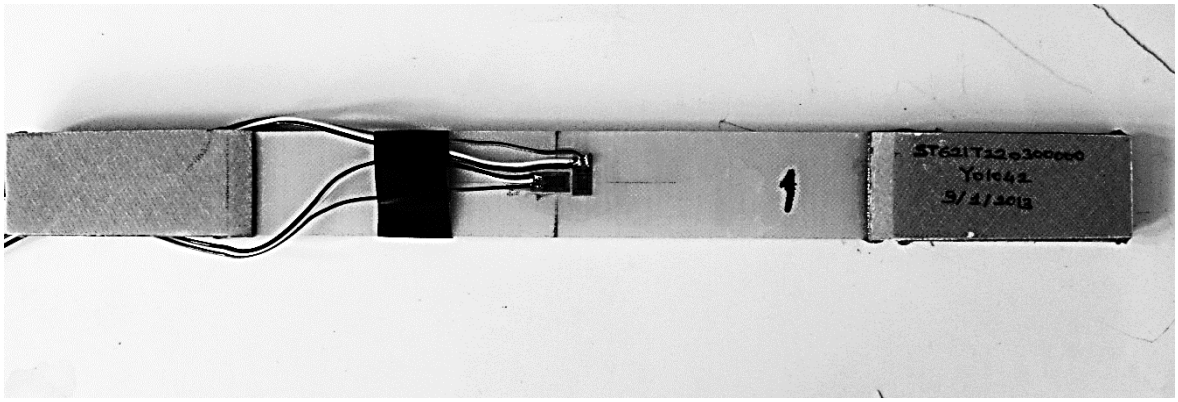

Figure 19: Transverse tension test specimen

A total of 4 longitudinal and 3 transverse glass specimens, and 12 carbon specimens, 6 from each, are tested. The test speed is set as 2 mm/min and data is collected with 5 Hz frequency. Modulus and Poisson's ratio calculations are performed by considering 0.2% and 0.5% longitudinal strain points. Stress-strain and load-extension graph of glass fiber longitudinal tension test specimens are presented in Figure 20 and Figure 21, respectively.

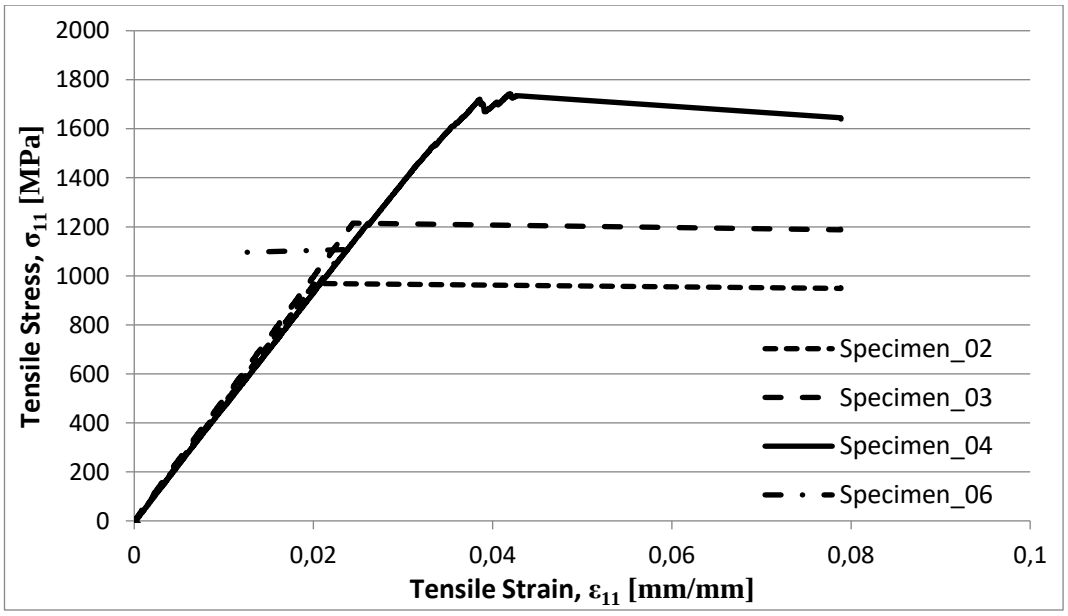

Figure 20: Tensile stress versus tensile strain graph of glass fiber longitudinal tension test specimens

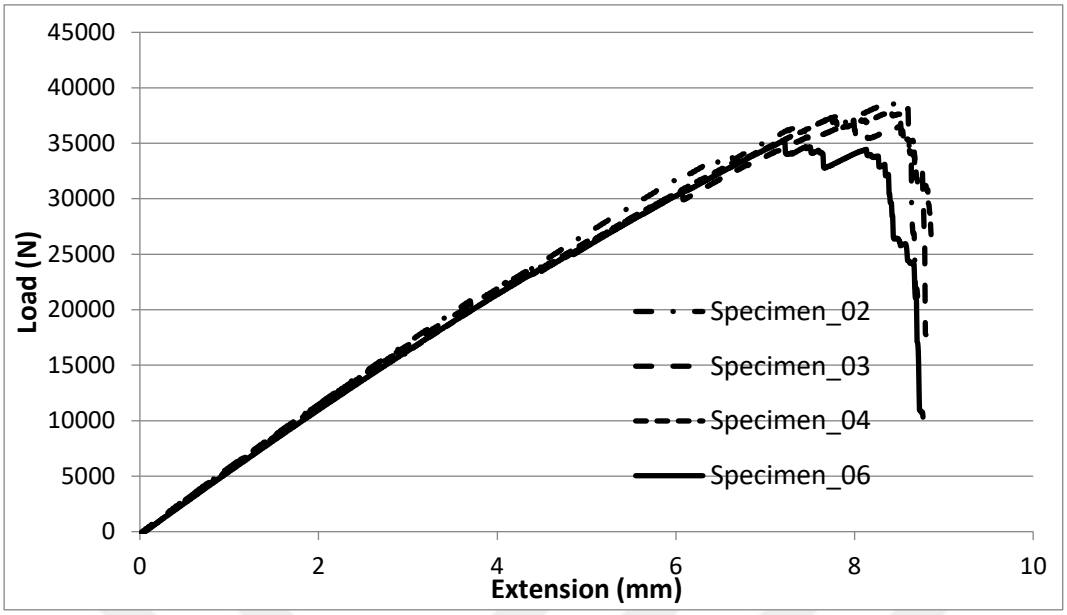

Figure 21: Load versus extension graph of glass fiber longitudinal tension test specimens

$$E_{11} = \frac{\Delta\sigma_{11}}{\Delta\epsilon_{11}} \tag{36a}$$

$$\nu_{12} = \frac{\Delta\epsilon_{22}}{\Delta\epsilon_{11}} \tag{1b}$$

UTS is taken from the test data, where the ultimate load is measured, and the ultimate strain is calculated as follows:

$$\epsilon = \frac{UTS}{E} \tag{37}$$

For the longitudinal test of both materials, the failure is observed as exploding of specimen at the ultimate load as seen in Figure 22. This type of failure is an accepted one according to ASTM D3039 standard.

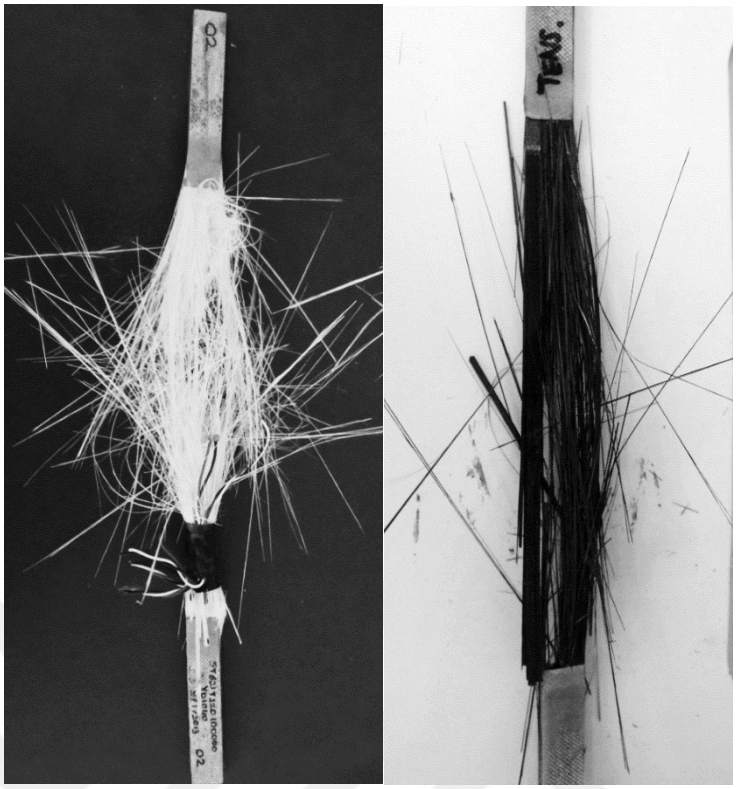

Figure 22: Longitudinal tension test specimens after failure

On the other hand, transverse tension specimens are failed laterally by matrix failure at an angle as presented in Figure 23. This is also an accepted failure type for ASTM D3039 Tensile Test Standard.

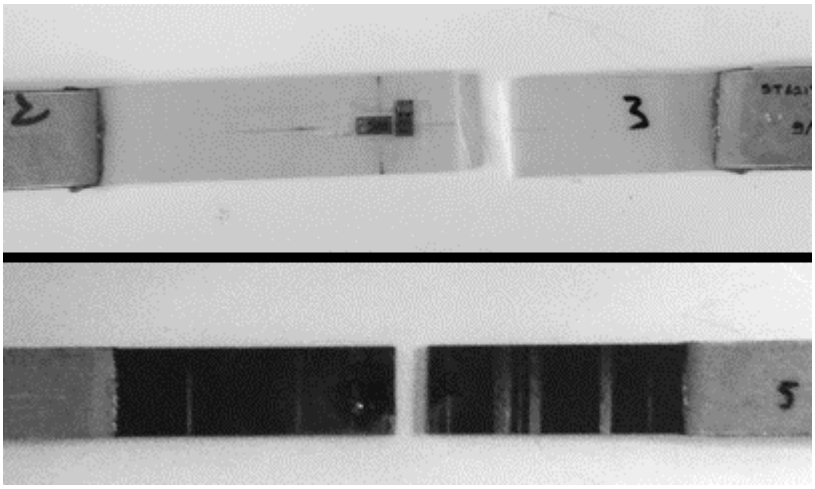

Figure 23: Transverse tension test specimens after testing

Main problem during tests is that, attaching strain gages on the surface of FRPs is difficult. When a few fibers under the gage is failed but the laminate still carries load, the gage cannot measure strain correctly. This problem can be observed in Figure 20; however, modulus calculations are not affected, since 0.2% and 0.5% strain values are used.

3.1.2 Compression Tests

In order to find the ultimate compressive stress and secant modulus of materials, longitudinal and transverse compression tests are performed according to DIN EN2850 Standard [38]. Type B option is used for preparation of specimens and testing apparatus. 1 mm/min constant head speed is used and data is collected with 5 Hz frequency. For longitudinal compression tests, two glass and three carbon specimens are tested. Specimens failed by crushing of plies at mid-section as shown in Figure 24. For longitudinal specimens, since the ultimate load is high, heads (where the specimen and test machine have a contact) of the first and second specimens are crushed before the failure in the gage region. In order to avoid this problem, metallic caps are attached to the heads to cover and protect them. This method is observed to be acceptable and the tests are successfully completed.

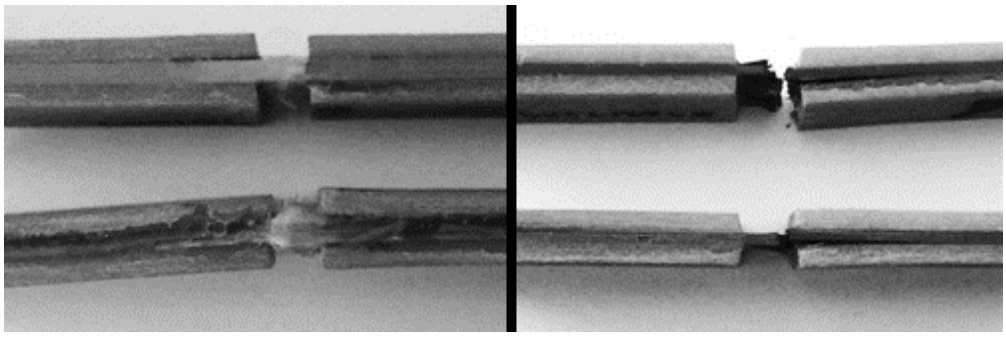

Figure 24: Longitudinal specimens after compression test

For transverse compression tests, four glass and five carbon specimens are tested, and failure surfaces with 45° angle plane is observed for all specimens. One of the failed specimens is presented in Figure 25.

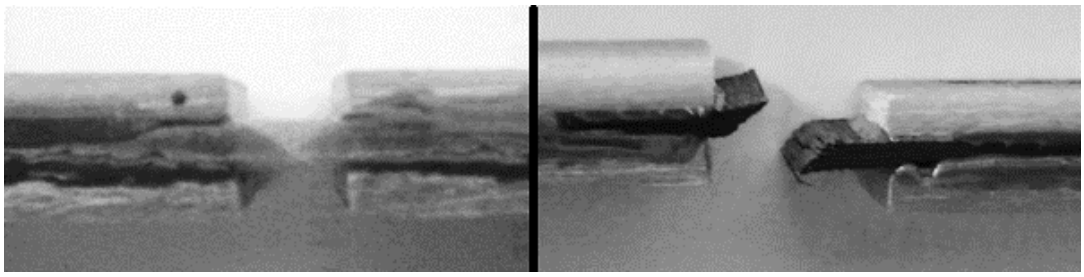

Figure 25: Transverse specimens after compression test

Load versus extension graph is given in Figure 26. Ultimate point is used to determine compressive strength and compressive stress, σ_C, compressive strain, ϵ_C, and the secant modulus, E, are calculated as follows:

$$\sigma_c = \frac{P}{w \cdot t} \tag{38a}$$

$$\varepsilon_c = \frac{\sigma_c}{l} \tag{3b}$$

$$E = \frac{\sigma_C|_{\epsilon=6\%} - \sigma_C|_{\epsilon=2\%}}{0.06 - 0.02} \tag{3c}$$

where P = Load at any point

w = Width of specimen

t = Thickness of specimen

l = Gage length of specimen

$\sigma_C|_{\epsilon=6\%}$ and $\sigma_C|_{\epsilon=2\%}$ = Stresses at 6% and 2% strain points, respectively

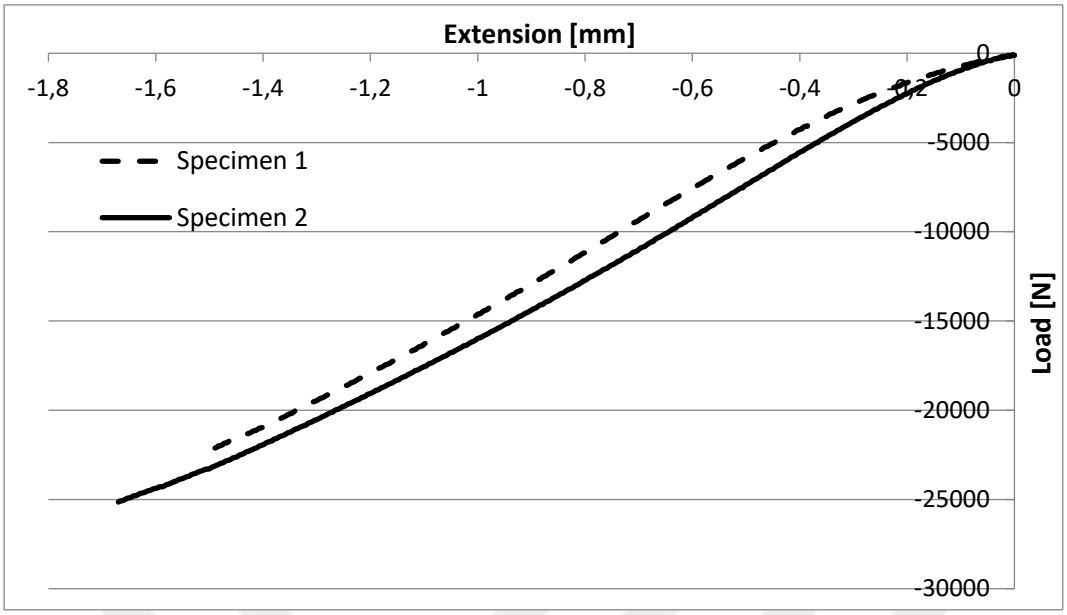

Figure 26: Load versus extension graph of glass fiber longitudinal compression test

3.1.3 In-Plane Shear Tests

In-plane shear characteristics of materials is determined with the tension tests of ±45° laminate; which consists of +45° and -45°, balanced and symmetric plies [39]. In this part of the material characterization study, 5 glass and 6 carbon fiber specimens are tested according to ASTM D-3518 Standard. In-plane shear modulus, G_{12}, is calculated with the data taken from tests which is presented in Figure 28. In Figure 27, the geometry of the in-plane shear specimen is presented.

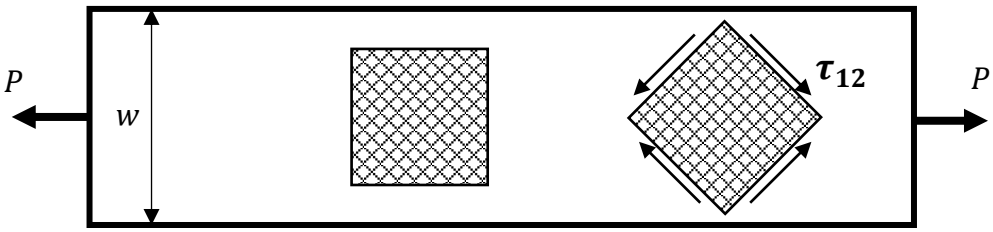

Figure 27: Geometry of in-plane shear specimen

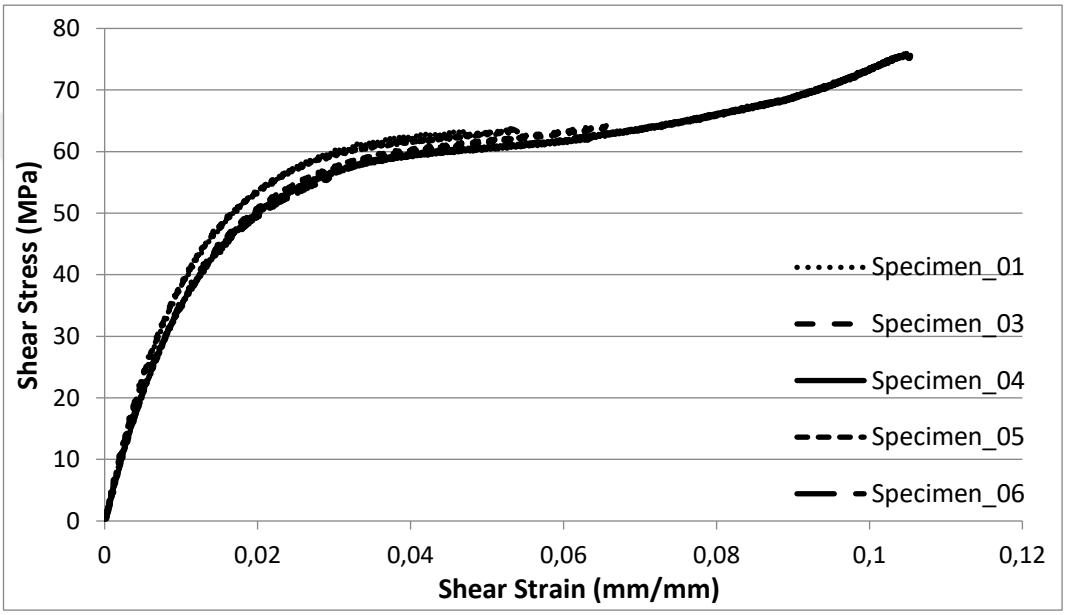

Figure 28: Shear stress versus shear strain graph of glass fiber in-plane shear test

$$\tau_{12} = \frac{P}{t \cdot w} \tag{39a}$$

$$\gamma_{12} = \tau_1 - \tau_2 \tag{4b}$$

The modulus is calculated between 0.2% and 0.6% strain points.

$$G_{12} = \frac{\Delta\tau_{12}}{\Delta\gamma_{12}} \tag{40}$$

Where $\tau_{12}$and γ_{12} are in-plane shear stress and strain, respectively.

The ultimate in-plane shear stress, $\tau_{12,ult}$, is determined from the strain gage data. Since the strain gage is limited with 5% strain, the ultimate shear strain is taken as 5% strain if the recorded value is greater than that. For all specimens, a failure in the form of 45° is observed close to tabs as shown in Figure 29. According to ASTM D3518, this type of failure is accepted if it is not within the tab zone itself.

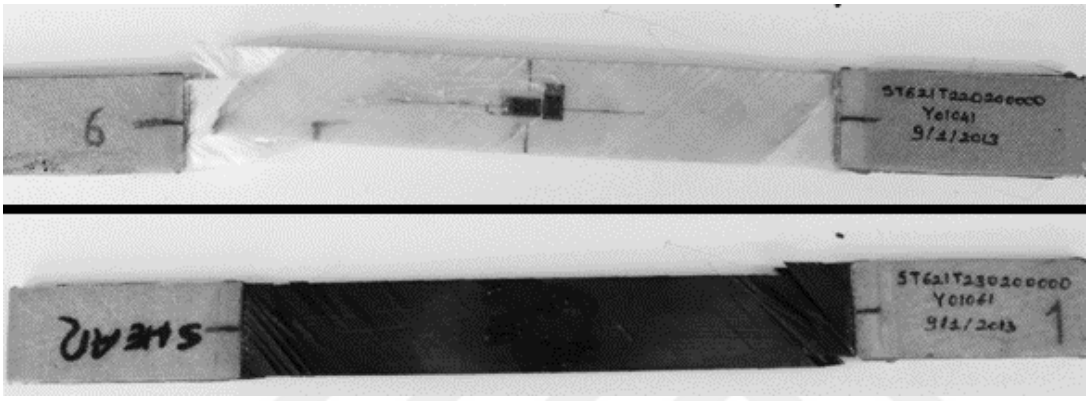

Figure 29: In-plane shear test specimens after failure

3.1.4 Open Hole Tension (OHT) Tests

In this section, tension tests aiming to investigate the static characteristics of the specimens with a hole is presented. The specimens are manufactured by drilling a hole in the middle. An OHT specimen is presented in Figure 30.

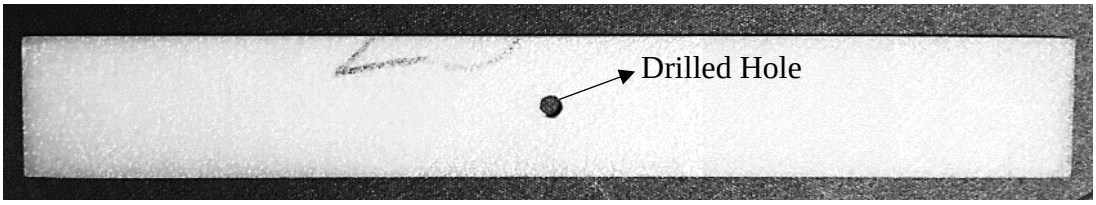

Figure 30: OHT specimen

Displacement controlled tests are conducted with a speed of 2 mm/min which is given in the ASTM D5766 standard [40]. The required grip pressure is given in the manual of the test machine. Therefore, a grip pressure of 20-bars is applied considering the anticipated maximum load. First trials showed that it is not adequate for a proper grip, thus then 70-bars grip pressure is decided by trial and error.

Since holes cause fiber discontinuities and in turn some delaminations, it is important to examine the open hole characteristics of laminates. So, 5 carbon fiber and 6 glass fiber hybrid laminates with holes are examined within this test program. No strain gage is used in this test, only load-displacement data is collected with the help of test machine's software and presented in Figure 31. The data is used to determine the ultimate tensile strength values for open hole specimens.

All specimens failed with 45° delamination around holes as can be observed from Figure 32.

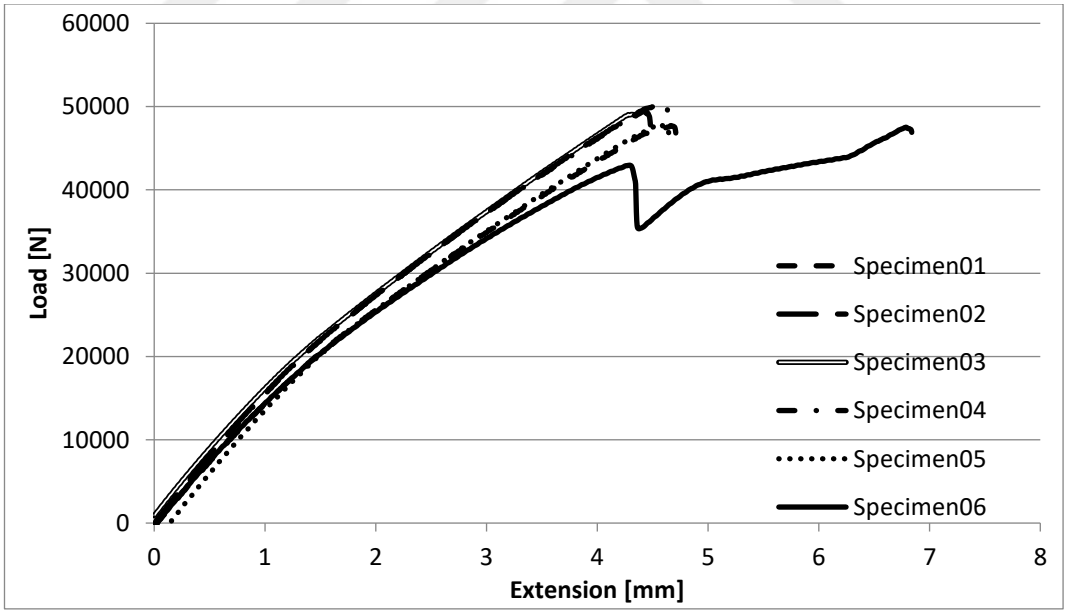

Figure 31: Load versus extension graph of glass fiber OHT test

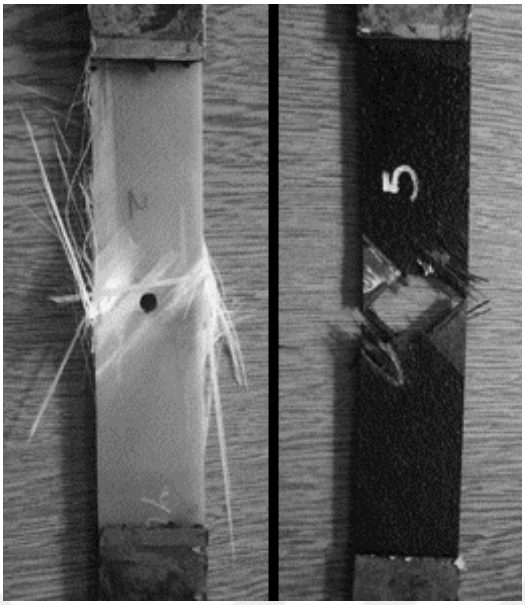

Figure 32: Open hole tension test specimens after failure

3.1.5 Open Hole Compression (OHC) Tests

In this section, compression tests for investigating the static compression characteristics of the specimens with a hole are explained. The compression load is applied to the specimens with the actuator of the testing machine. The tests are conducted in a displacement controlled manner with a speed of 0.5 mm/min as described in DIN EN6036 standard [41]. For this test, a grip pressure of 50-bars is

used. The test data is presented in and the ultimate load is determined to calculate the ultimate compressive stress for open hole specimens.

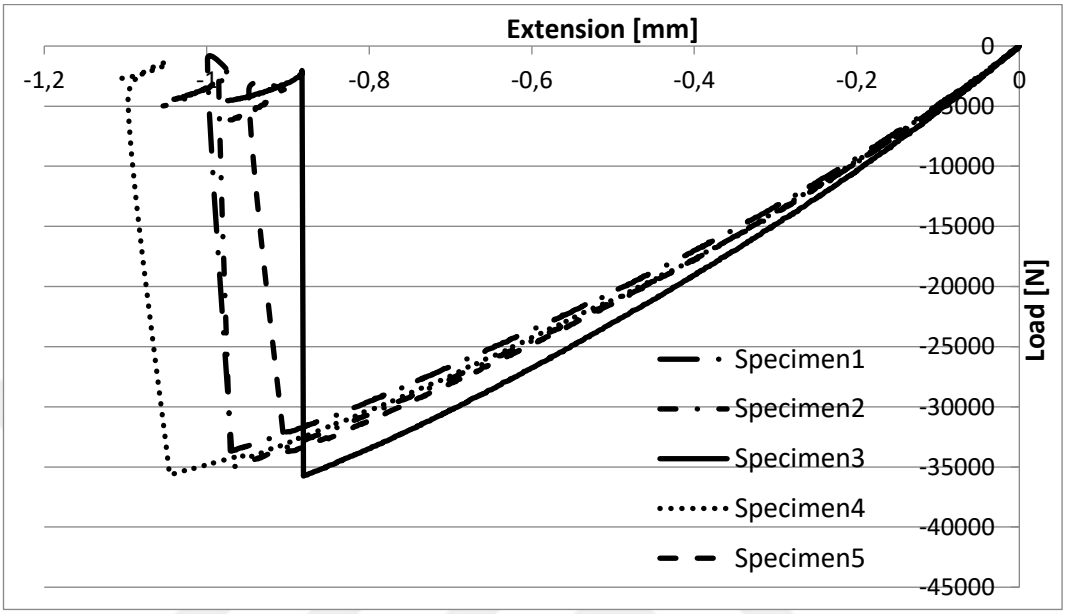

Figure 33: Load versus extension graph of glass fiber OHC test

All specimens failed with a 45° sudden crush and delamination around the hole section as presented in Figure 34.

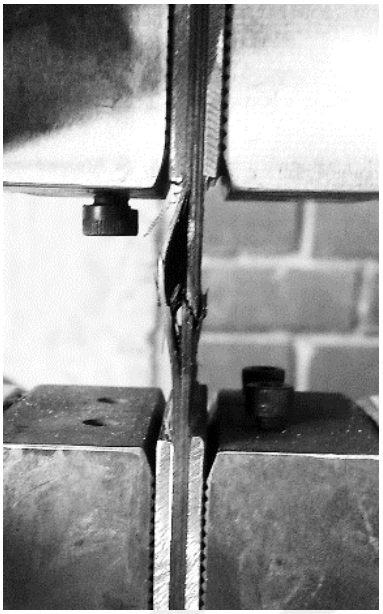

Figure 34: OHC specimen after failure

3.1.6 Bearing Tests

In this section, bearing tests for investigating the bearing response of materials are explained. Load is applied to the bearing specimens with the actuator of testing machine. The same displacement controlled test system is used here with a speed of 2 mm/min as given in the standard [42].

Specimens are attached to the apparatus as explained in the standard, from its hole by a pin having the same diameter with hole, which means one grip pulling the apparatus while the other one pulling the specimen. By that way, a bearing load was applied by the pin to the hole surface. A video extensometer is used for measuring the relative

motion of the specimen and apparatus, so bearing strain is measured. Test setup is presented in Figure 35.

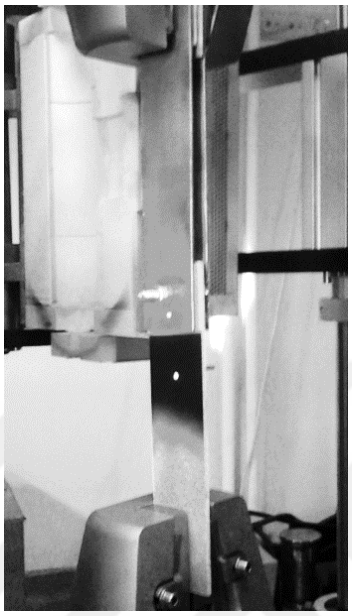

Figure 35: Bearing test setup

By using the software, extension, load, and strain from extensometer data collected with a rate of 5 hertz. Stress-Strain data is given in Figure 36 for five glass fiber bearing specimens.

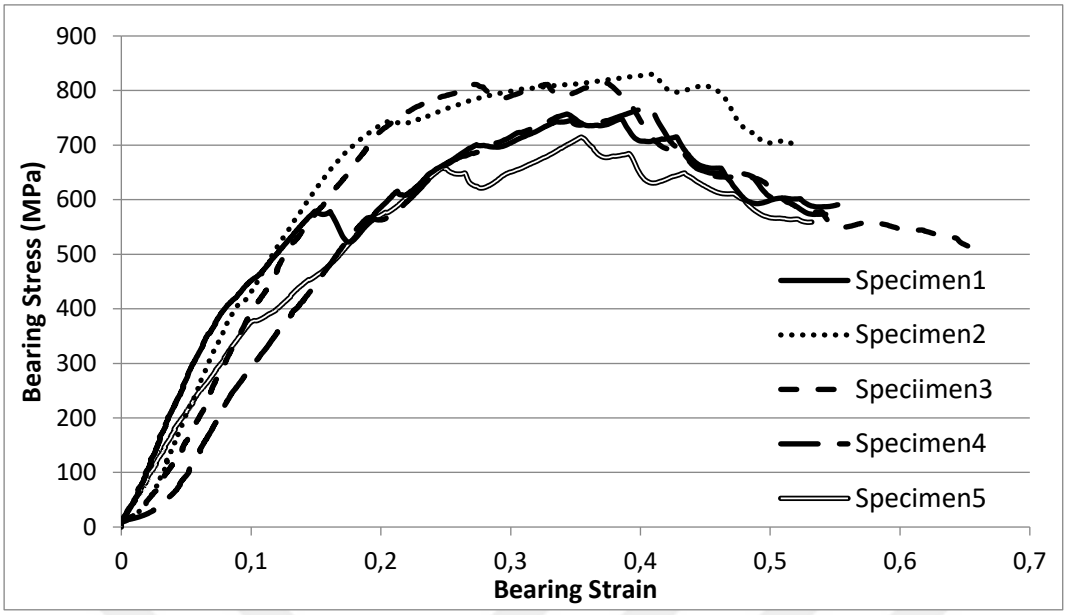

Figure 36: Bearing stress versus bearing strain graph of glass fiber bearing test

The parameters defined in the standard is given as follows,

$$edge\ distance\ ratio = \frac{e}{D} = \frac{g + D/2}{D} \tag{41}$$

where g= distance from the hole edge to the specimen end

D= hole diameter

$$\sigma_i^{br} = \frac{P_i}{D \cdot h} \tag{42}$$

where P_i= force at i^{th} data point

h= thickness

σ_i^{br} = bearing stress at i^{th} data point

$$E_{br} = \frac{\Delta\sigma^{br}}{\Delta\varepsilon^{br}} \tag{43}$$

E_{br} = Bearing Chord Stiffness

3.2 Fracture Toughness Tests

Properties of composite materials may change during service. Even moderately severe environmental conditions may sometime cause defects and degrade material properties. Delamination is one of these defects [43]. It can also be caused during manufacturing including drilling and cutting. In order to get a reliable analysis model, the progression of delamination is to be determined. For this purpose, as a common practice, Mode I and Mode II fracture toughness tests are conducted to obtain the fracture energy of composite materials for tensile and shear loading, respectively. These fracture modes are presented in Figure 37.

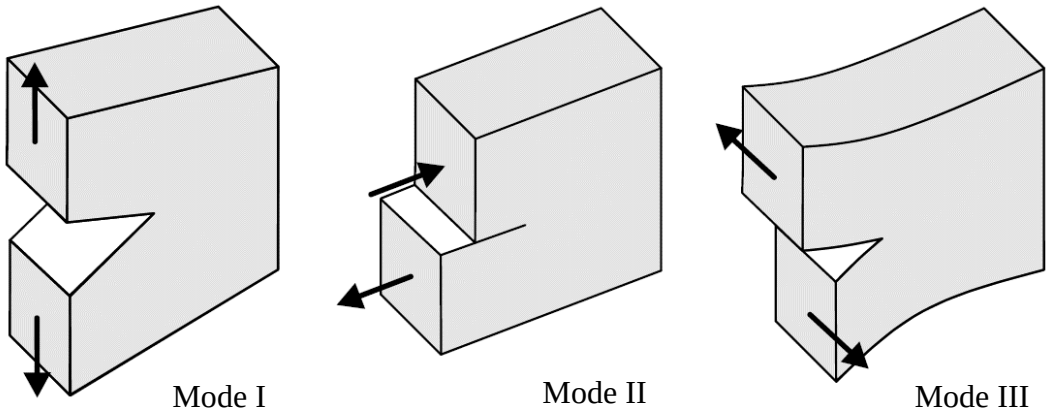

Figure 37: Fracture modes [44]

3.2.1 Mode I Fracture Toughness Tests

In order to determine Mode I fracture toughness, G_{IC}, of continuous fiber reinforced composite materials, DCB (Double Cantilever Beam) specimens are tested according to ASTM D5528 standard [45]. Since the delamination is one of the major weaknesses

of composite structures, determining opening mode fracture toughness is essential for developing a valid delamination failure criteria [45].

As mentioned in the standard, unidirectional DCB specimens with an artificial (induced) delamination is loaded from the hinges in the opening direction. The delamination tip in the specimen is marked and a ruler is attached just under it to measure the current crack length. A video camera is also used to focus on the crack tip. Data in the form of the crack length, a, and load, P, is recorded for each crack growth, Δa, which is usually in the order of a millimeter. The test setup is presented in Figure 38.

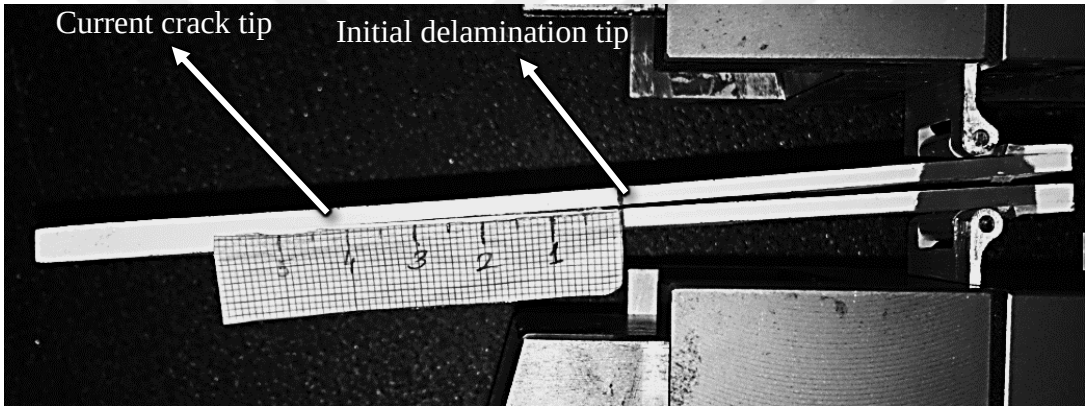

Figure 38: DCB test setup

Three different calculation methods for G_{Ic} is explained in the standard. These are Modified Beam Theory (MBT), Compliance Calibration (CC), and Modified Compliance Calibration (MCC). For further explanation of these methods, a calculation for a glass specimen is shown as follows:

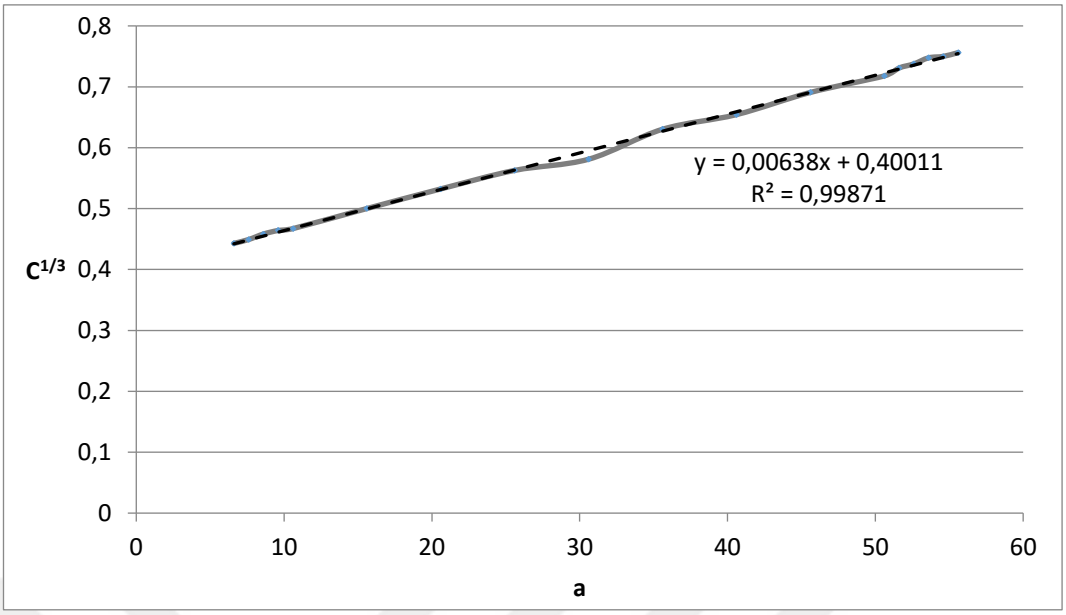

Figure 39: Plot for calculation of MBT

MBT can be calculated from:

$$G_{I\_MBT} = \frac{3P\delta}{2b(a + |\Delta|)} \tag{44}$$

where: δ= Load point displacement

b= Width of the specimen

Δ= Offset value which is shown in Figure 40.

C= Compliance (δ/P)

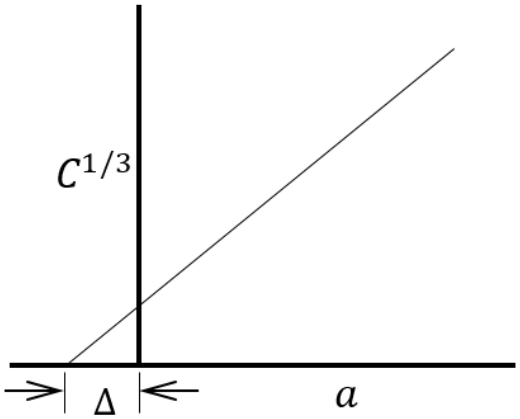

Figure 40: Geometry of Δ [45]

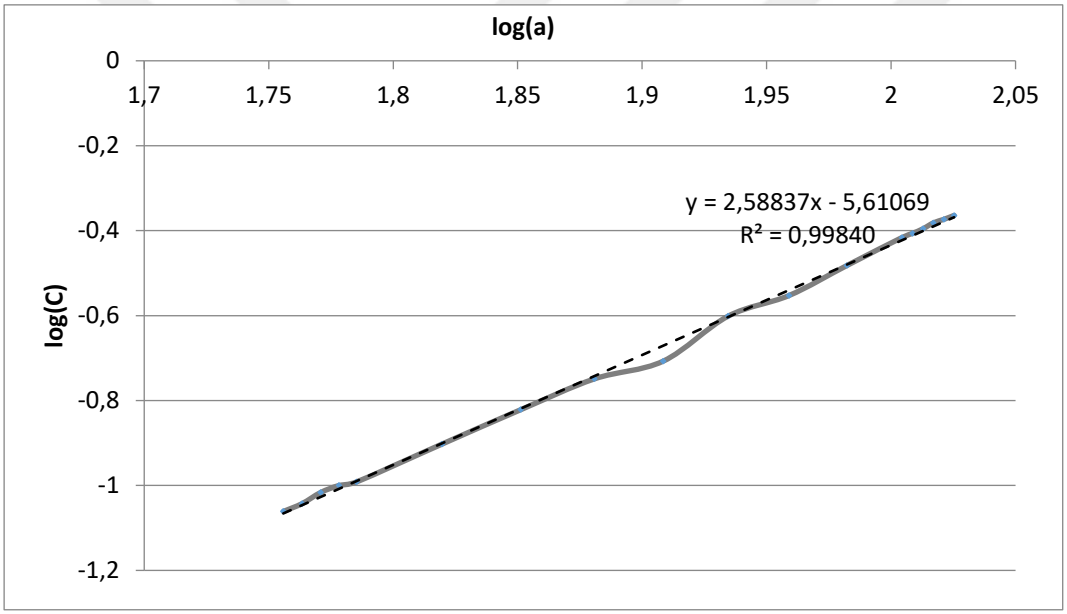

Figure 41: Plot for calculation of CC

CC can be calculated as:

$$G_{I\_CC} = \frac{nP\delta}{2ba} \tag{45}$$

where, n is the slope of least square fit of log(a) versus log(C).

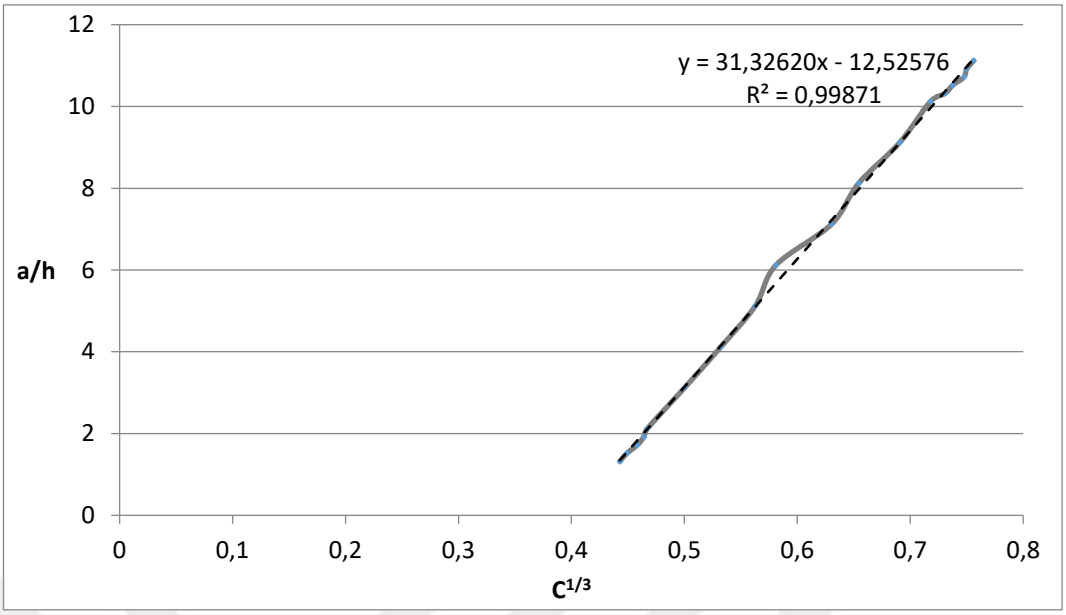

Figure 42: Plot for calculation of MCC

MCC can be determined from:

$$G_{I\_MCC} = \frac{3P^2C^{2/3}}{2A_1bh} \tag{46}$$

where, A_1 is slope the graph in Figure 17.

As seen in Figure 43, MBT, CC and MCC results have a perfect match. Since least squares fitting for the experimental data is used for calculation, all methods give approximate results.

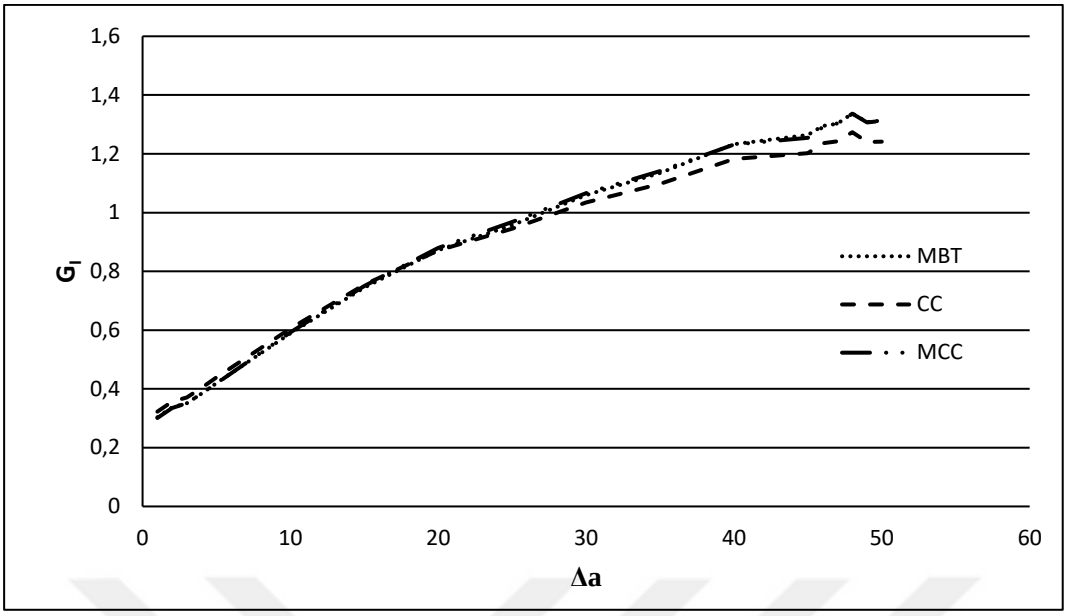

Figure 43: G_I values for each methods

3.2.2 Mode II Fracture Toughness Tests

As explained in ASTM D7905 [46] standard ENF tests are performed to obtain Mode II inter-laminar fracture toughness of glass and carbon fiber laminates, with Mode II type of shear loading. Figure 44 shows the test setup.

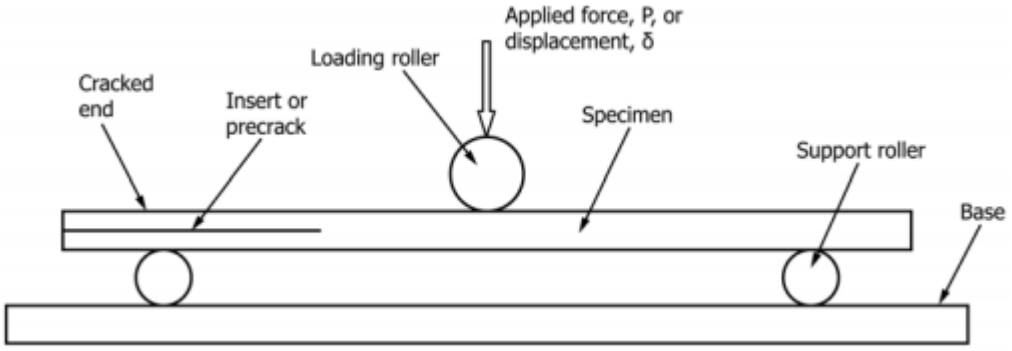

Figure 44: ENF Test Setup [46]

As presented in the figure, load is applied to the mid-section of specimen by a roller. The test is performed with a displacement rate of 0.6 mm/min. Distance between supports is arranged as 100 mm. As shown in Figure 45, the initial crack tip is marked and a ruler is attached to track the crack growth. A camera coupled with a light source is also utilized to monitor the crack tip more accurately.

The ENF test specimen is continuously loaded until the load started to increase just after the delamination growth, then it is unloaded by ensuring that the load-displacement curve reaches the starting point.

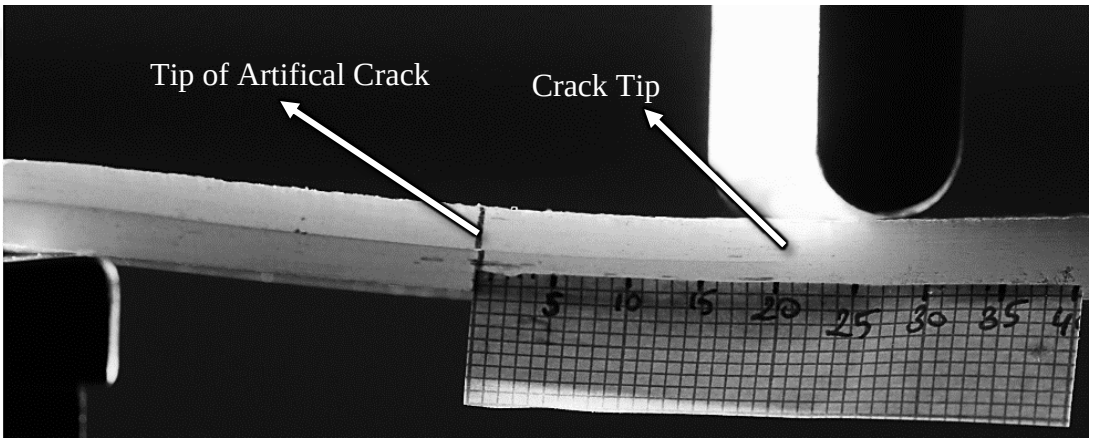

Figure 45: ENF testing of glass specimen

4 glass and 7 carbon fiber specimens are tested. The load and roller displacement data is collected with a rate of 5 Hertz.

The fracture toughness is calculated with the following formula:

$$G_{IIC} = \frac{a_0^2 \cdot P_{max} \cdot \delta_{max}}{2W(D^3 + 3a_0^2)} \quad (47)$$

a_0= Initial crack length

P_{max}= Maximum load

δ_{max}= Maximum displacement

D= Distance between supports

The load displacement curve of glass specimens are presented in Figure 46.

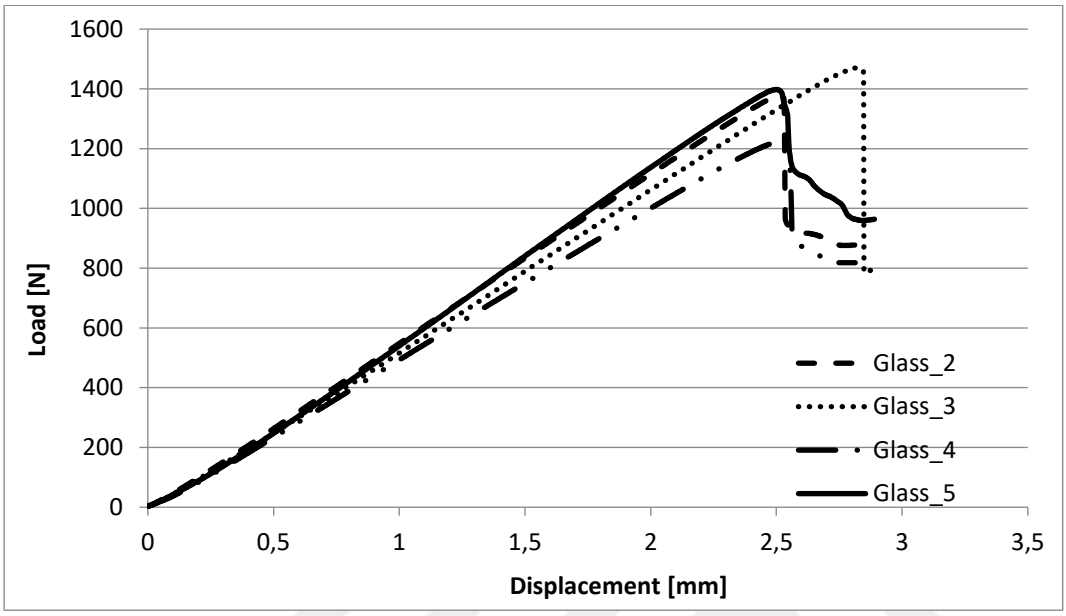

Figure 46: Load - displacement plot of glass ENF tests

3.3 Test Results

Test results from various tests are presented in Tables Table 6-Table 7Table 8.

Table 6: Results of tension and in-plane shear tests

	Glass Fiber Direction	**Glass Transverse Direction**	**Carbon Fiber Direction**	**Carbon Transverse Direction**
E **[GPa]**	48.6	10.3	141.7	8.9
ν_{12}	0.29	-	0.31	-
ϵ_{ult} **[%]**	0.36	0.051	0.16	0.050
σ_{ult} **(UTS) [MPa]**	1764	52.6	2200	44.1
G_{12} **[GPa]**	3.96		4.28	
τ_{ult} **[MPa]**	90.2		81.7	
γ_{eff} **[%]**	0.23		0.19	
γ_{ult} **[%]**	0.50		0.50	

Table 7: Compression test results

	Glass Fiber Direction	**Glass Transverse Direction**	**Carbon Fiber Direction**	**Carbon Transverse Direction**
E **[MPa]**	2475.6	2642.88	6189.83	2858.83
σ **(Ult. Comp. Strength) [MPa]**	1046.23	186.67	1292.20	194.59

Table 8: Bearing test results

	G/Ep	**C/Ep**
E_{br} **(Chord Stiffness) [MPa]**	4592	3755

All test activities are completed with reasonable results according to standards used and necessary material properties are determined. Material properties obtained are compared with the results of a composite material from the materials database of Turkish Aerospace Industries (TAI), which has the same fiber, S2-Glass with a different matrix. It is observed that properties in fiber direction especially match for both material systems.

A number of problems are worth mentioning. Starting with the gripping problem, it can sometimes causes crushing of specimens easily, since composite materials are known to be quite brittle. In order to prevent this problem, the end of the specimens should be reinforced with tabs, appropriately. Another important problem is, the difficulty of perfectly bounding the strain gages on composite materials and a result gages may disengage from the surface at a very early stage of loading. It takes time to gain experience on the proper gage bonding.

CHAPTER 4

NUMERICAL ANALYSIS

Finite element is an approximation method by discretizing the structure into finite number of elements. It is assumed that as the number of elements goes to infinity, then the solution converges to exact solution. Finite element approach approximates the solution by building equations to solve unknown parameters for each elements. Then, by combining equations of the elements and applying boundary conditions, the approximate solution is obtained. Today, so many commercial software packages are available for finite element modelling. These programs allow to make non-linear analysis. These computer aided engineering (CAE) systems generally follow three steps. First, model is needed as input to software which includes geometry, material properties element formulation, boundary conditions and loads. Second, software solves equilibrium equations to obtain displacements. Finally, required outputs like stress, strain, failure conditions are derived [47].

In this chapter, finite element method which is used to analyze the composite plate which is loaded by a pin. Different models are built to understand effect of mesh (shape and size), step time, cohesive layer and degradation types. Results of these models are compared with experimental data. The composite plate consists of nineteen layers with $[+45/-45/0_7/\bar{0}]_S$ stacking and has the thickness of $4.37\,mm$ (Each layer $0.23\,mm$). This plate is loaded by a $42\,mm$ diameter pin. The plate is modelled such that the hole has enough distance from edges. Geometry of the plate is shown in Figure 47. Since the pin applies the load in x direction, right side of the hole is kept longer to prevent shear-out or cleavage type of failure [42].

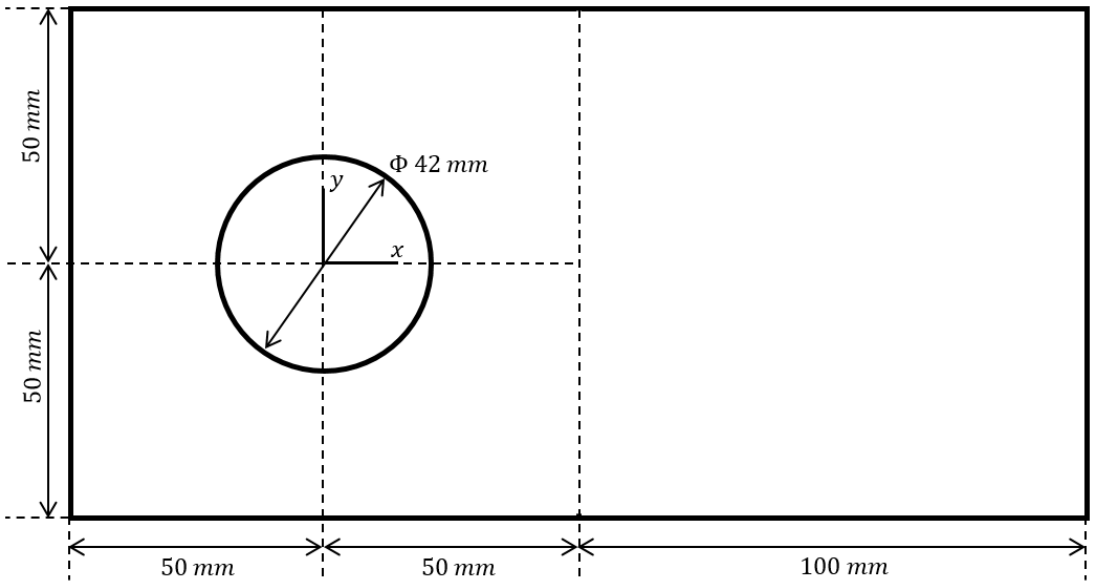

Figure 47: Geometry of the plate

4.1 Numerical Method

Two type of analysis are used for numerical solutions. One is the implicit method which find a solution by solving a function consists of the current state and a time increment later. On the other hand, the method which is called as explicit uses a function consists of the current state and solves for the next one. Explicit methods require small time increments to estimate the next condition; so, especially for linear and small models, explicit method results in unnecessary extra computation. Implicit methods require more iteration to find a solution but use greater time increments. However, for non-linear and complicated models, implicit method may not converge to a solution.

Commercial software, Abaqus™, offers both types of analysis. According to Abaqus™ User Manual [48], explicit model should be used for large problems and problems with nonlinearities. Even, the explicit model requires small time increments; the analysis cost increases with problem size linearly. On the other hand, for the implicit model, cost of the analysis increases rapidly, and convergence problem may

happen. Since, analysis of FRPs, especially with progressive damage, is non-linear; Abaqus™/Explicit is used for modeling.

4.2 Element Type

Another important modelling parameter is choosing which type of element is used. Abaqus™ offers solid, conventional shell and continuum shell modelling for composite layups. However, Abaqus™/Explicit allows only a single homogeneous material and solid composite elements can only have displacement degrees of freedom [49]. Another option is conventional shell elements, which does not have a geometrical thickness but the thickness is defined as section parameter. For conventional shell composite layup, only the reference surface is discretized for each ply [49]. On the other hand, fully discretization is possible for each ply by using the continuum shell composite layup. As mentioned in Abaqus™/CAE User's Guide [49], the continuum shell element is more suitable for contact analysis since double-sided contact and thickness changes is considered. Geometrical representation of conventional and continuum shell elements is given in Figure 48. Under the light of this information, 8-node quadrilateral continuum shell element (SC8R) is assigned for composite layup.

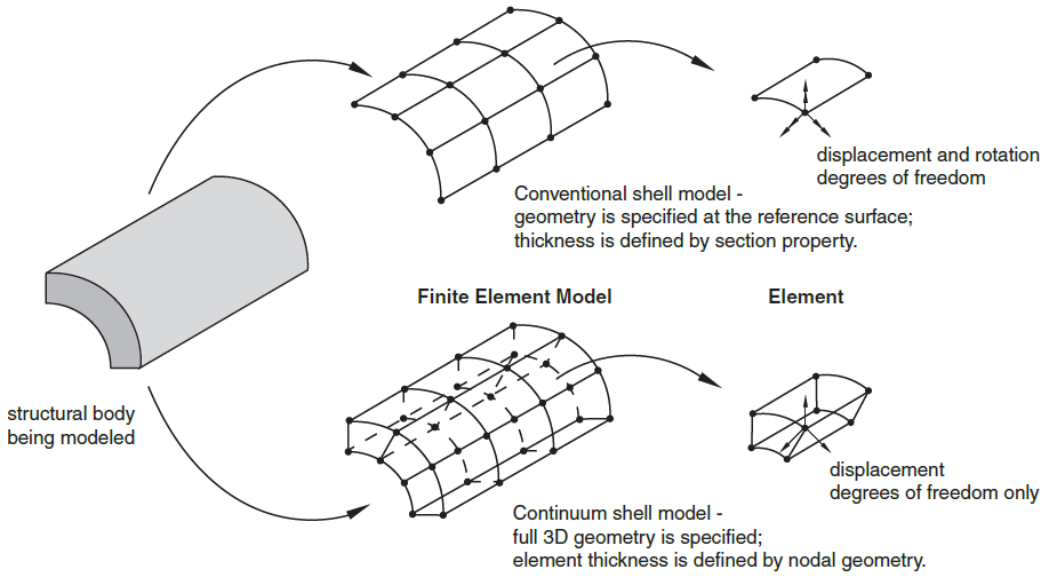

Figure 48: Conventional and continuum shell elements [50]

4.3 Material Properties

The material properties which are used for modelling is determined by coupon tests. This material characterization study is explained in Chapter 3. The properties for composite with S2 Glass fiber and MTM49L resin is given in Table 9. For the properties Abaqus™ sign convention is used; so, strength and modulus values are given in MPa and density is in $tonne/mm^3$. Shear modulus is assumed equal for three directions, and transverse and longitudinal shear strength are taken as equal.

Table 9: Material Properties

ρ	$1.857 \cdot 10^{-9}$
E_{XX}	48600
E_{YY}	10300
G_{XY}	3960
X_T	1764
X_C	1046
Y_T	52.6
Y_C	186.67
S_{XY}	90.2
ν_{XY}	0.29

Another important material properties are fracture energies. Fracture energies for longitudinal tension (LTFE), longitudinal compression (LCFE), transverse tension (TTFE) and transverse compression (TCFE) are required for progressive failure. When the coupon tests which are presented in Chapter 3, failure is observed as a sudden crush. As can be seen in Figure 49, load increases linearly and failure happens suddenly without any significant softening.

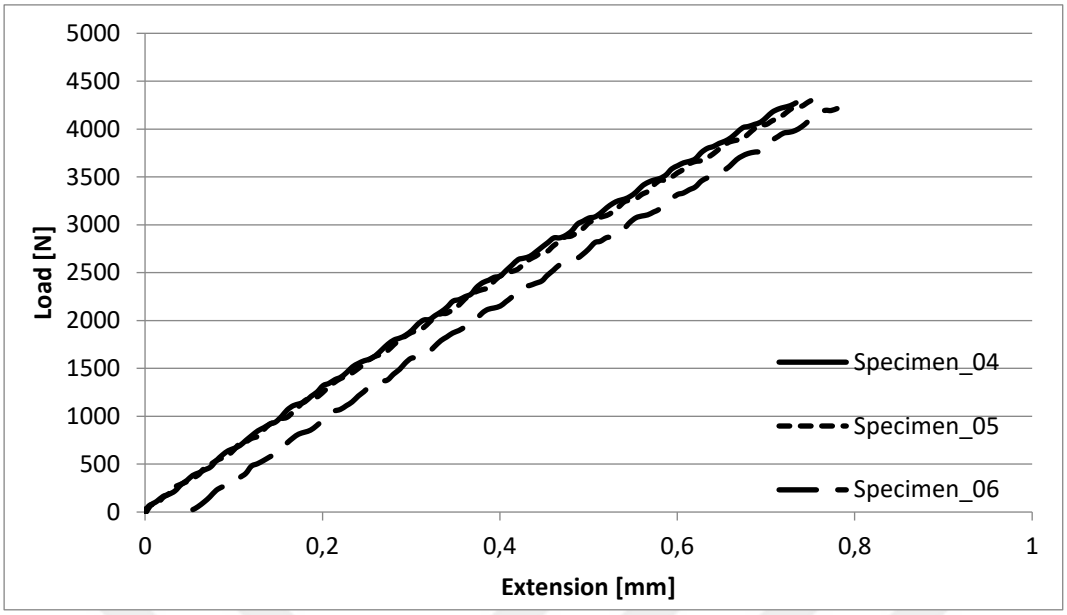

Figure 49: Load versus extension graph of transverse tension test

In order to determine fracture energies for almost sudden failure, an element is generated on Abaqus™ which has the side length of 0.5 mm and only one layer. By applying load to the element for fiber tension and compression, and transverse tension and compression, failure mechanism is observed clearly. Failure mechanisms are presented for longitudinal direction in Figure 50, and for transverse direction in Figure 51. Fracture energies corresponding to this almost sudden failure condition is given in Table 10.

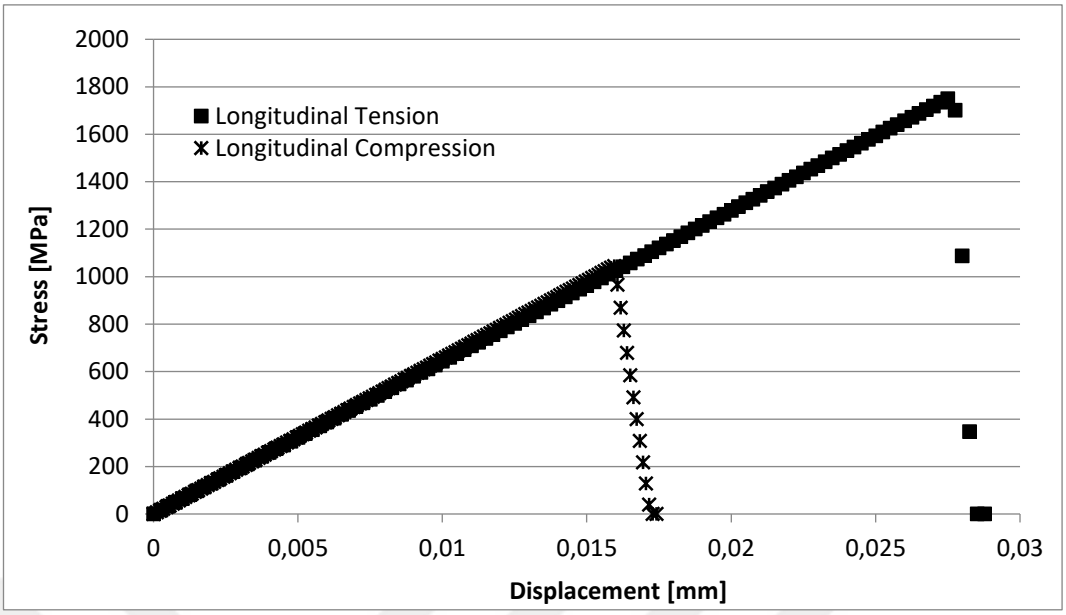

Figure 50: Failure mechanism for fiber

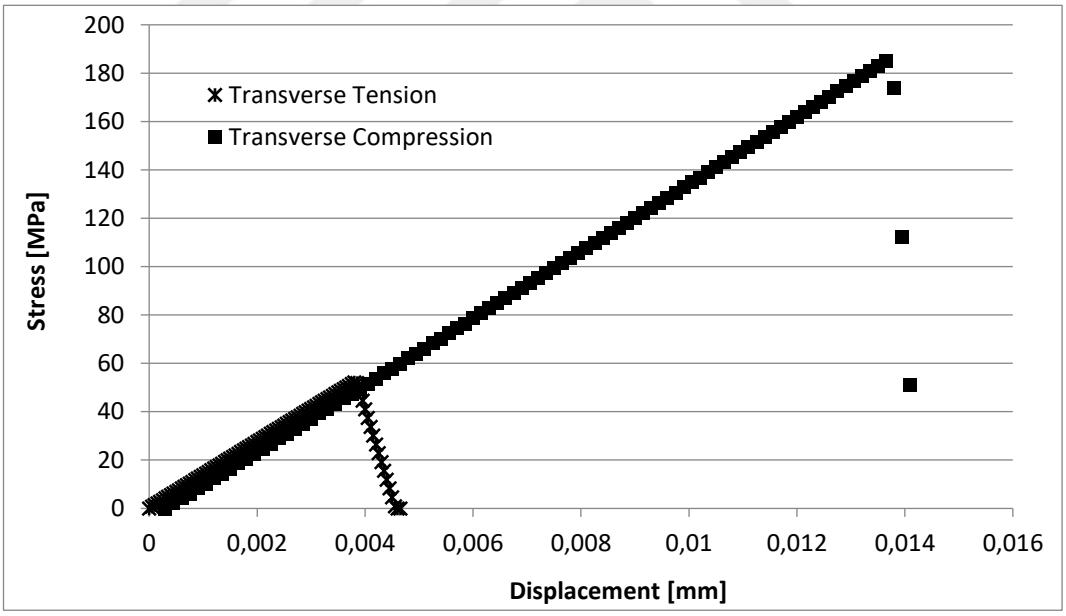

Figure 51: Failure mechanism for matrix

Table 10: Fracture energies [N/mm] for almost sudden failure

LTFE	LCFE	TTFE	TCFE
25	9	0.12	1.3

However, if the load versus displacement graph of bearing test, which is given in Figure 35, is examined; failure happens gradually and softening can be observed clearly. Since the failure observed in matrix for bearing tests, analysis are performed with higher fracture energies in transverse direction. So, three progressive failure cases are used in the models, which are shown in Table 11: Fracture energies [N/mm]

Table 11: Fracture energies [N/mm]

Case #	LTFE	LCFE	TTFE	TCFE
1	25	9	0.12	1.3
2	25	9	3	3
3	25	9	5	5

4.4 Mesh

The plate is divided into partitions from the dashed lines as shown in Figure 47 to be able to create fine and symmetric mesh around hole and coarse mesh at non-critical region. Two different mesh patterns are used to understand the effect of element geometry. In both models, 1 mm element size is used around holes. These two mesh patterns are presented in Figure 52. The composite plate is colored with green and the pin is colored with orange. For Mesh A, 78508 elements are created; and for Mesh B, 190912 elements are created. Element number is reduced by using coarse mesh at non-critical regions in Mesh A. By that way, run time gets shorter. Another advantage of Mesh A is that; elements around pin have better mesh uniformity. This is important because non-uniform elements may deform excessively before ultimate failure. On the other hand; the pin is undeformable and no data is taken from it; but mesh on the pin

should be fine enough to prevent element edges causing excessive deformations on the plate and the element size should be close to the one on the plate since they are in contact.

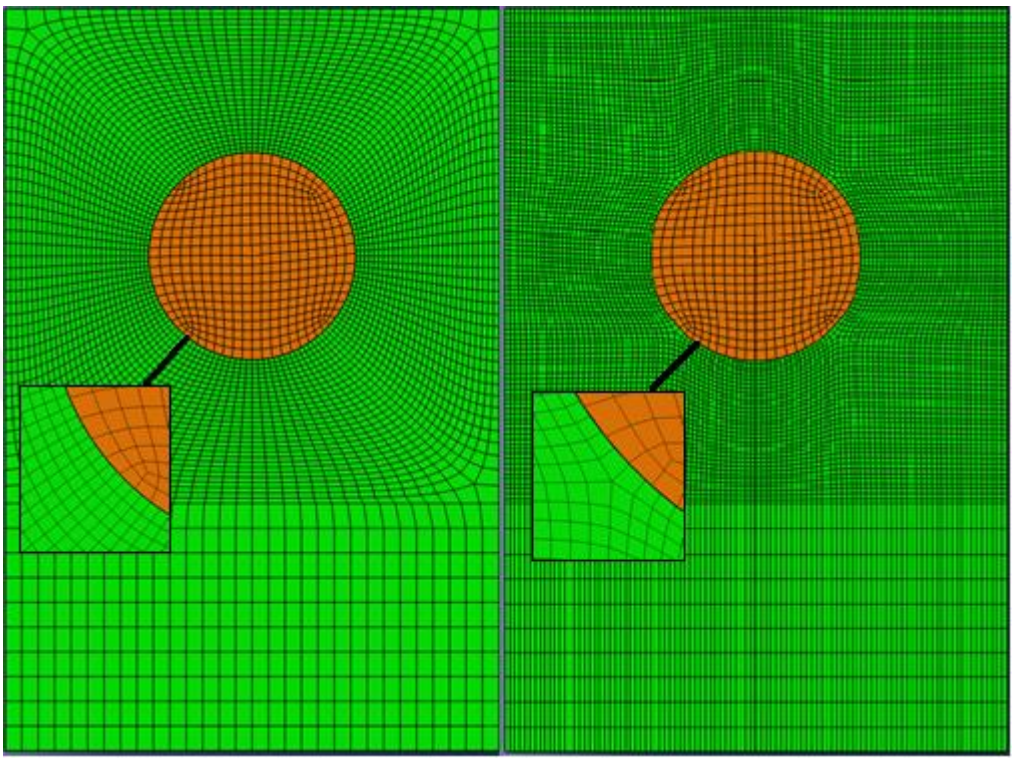

Figure 52: Mesh patterns: Mesh A (Left) Mesh B (Right)

As seen in Figure 53, two models give matching results. So, when the advantages are considered, it is decided to use Mesh A pattern for other models.

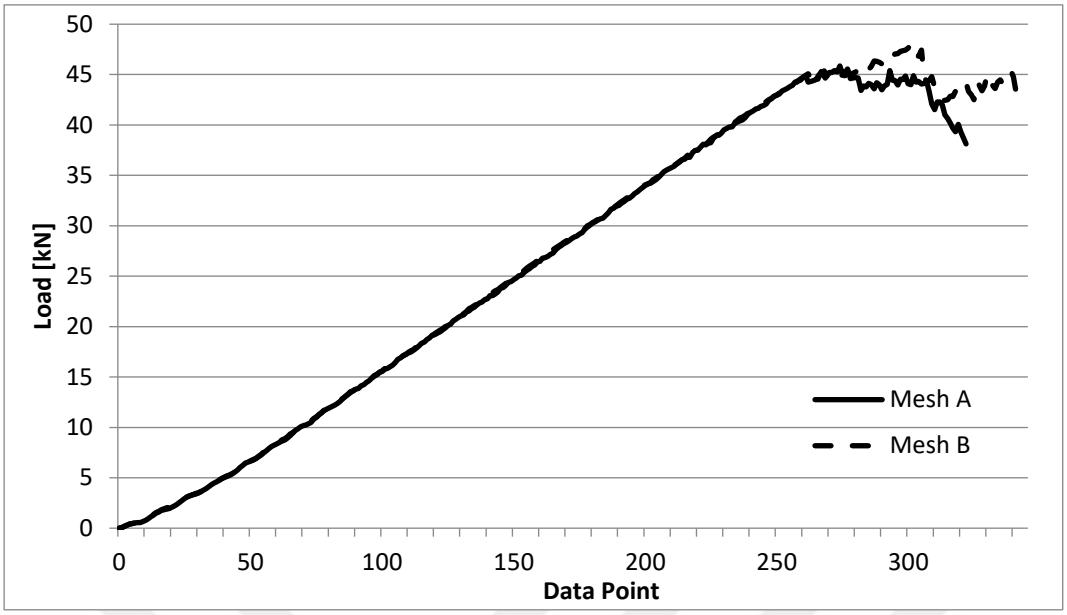

Figure 53: Force versus data point graph for two mesh patterns

Then, different mesh sizes are compared to find the optimum mesh size. Load versus displacement graph of the analysis with element sizes (ES) around the hole of $1\ mm, 0.75\ mm, 0.5\ mm$ are given in Figure 54. As seen from the graph that, analyses for ES: $0.75\ mm$ and $0.5\ mm$ have matching results. 324482 elements are generated for $0.5\ mm$ ES and 113164 elements are generated for $0.75\ mm$. Another important point is using $t = 0.005\ s$ is not appropriate for $0.5\ mm$ ES and does not give realistic results. The reason for this problem is that, for smaller elements required stable time increment is getting smaller [51]. So, $0.5\ mm$ ES is solved with $t = 0.02$. Then $0.5\ mm$ ES is chosen for the model, and presented in Figure 55.

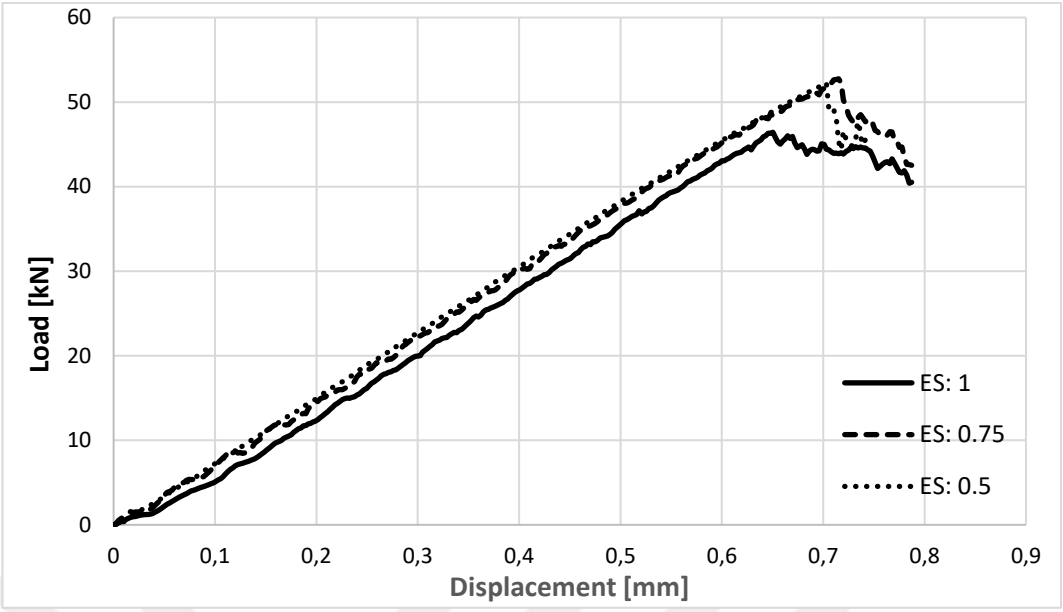

Figure 54: Load versus displacement graph for different element sizes

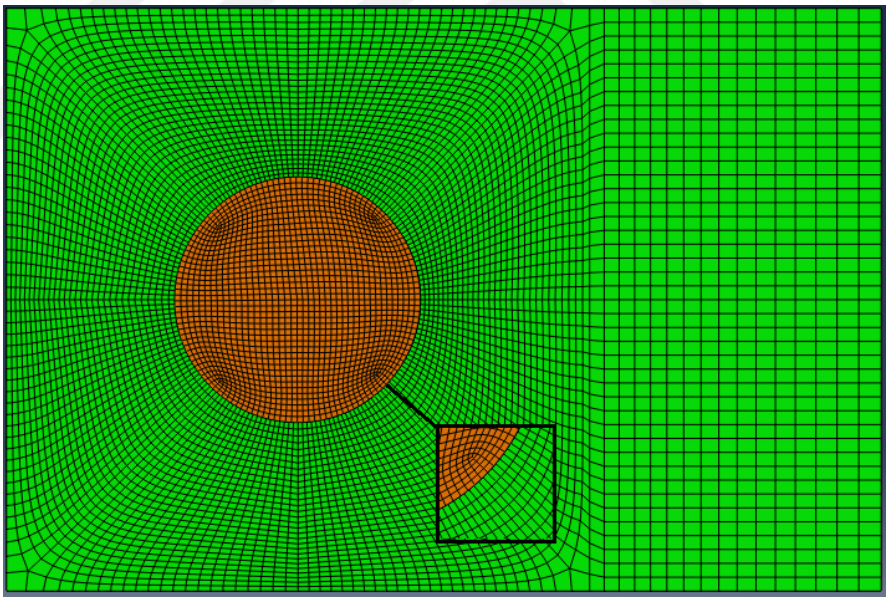

Figure 55: Model with 0.5 mm ES mesh

4.5 Step Time (T)

There are two important time parameters in Abaqus™ especially for dynamic-explicit analysis. First parameter is time increment, Δt, which is calculated by the software with following formula [48].

$$\Delta t \leq \min\left(L_e \sqrt{\frac{\rho}{\hat{\lambda} + 2\hat{\mu}}} \right) \tag{48}$$

where L_e is the characteristic length of the element, and $\hat{\lambda}$ and $\hat{\mu}$ are the effective Lame constants given as follows:

$$\hat{\lambda} = \frac{E\nu}{(1+\nu)(1-2\nu)} \tag{49}$$

$$\hat{\mu} = \frac{E}{2(1+\nu)} \tag{50}$$

As seen in (48-50), required Δt only depends on material properties. Abaqus™ have both automatic and fixed time increment options, and automatic time increment is used for analysis.

Second parameter is the step time, T, which is the artificial time span assigned to the analysis. For constant material properties, time increment is also constant and more iterations are needed for larger step time. By considering this situation run time of the analysis can be reduced by decreasing T. However, when T is decreased, displacement at each increment increases and

Another important parameter is the step time (T). Since the analysis are dynamic-explicit, time span of the analysis is important and in Abaqus™ velocity of the elements are effective on the results. Keeping the step time larger is safe but also increases run time. So, time dependency of the model is checked by running the analysis for different step times (0.01, 0.005, 0.002, 0.001 sec). As shown in Figure 56, the result of analyses with $T = 0.01$ and $T = 0.005$ are very close. However, when $T = 0.002$ force data starts to deviate; and for $T = 0.001$ this deviation

becomes more visible. The reason of this deviation can be understood from Figure 57. Oscillation in kinetic energy for the analyses with smaller t can be seen in the graph. After the ultimate failure instability is observed as expected. Even the elements are very small, when the rate of deformation gets higher inertia effects are included. So, this changes in kinetic energy results in deviations in load. This problem is addressed in Abaqus™ User Manual [48], as reducing time period, t, speeds up the analysis; so, increasing the speed too much causes errors due to inertia. As the result, $T = 0.005$ is determined as optimum step time and is used for analysis.

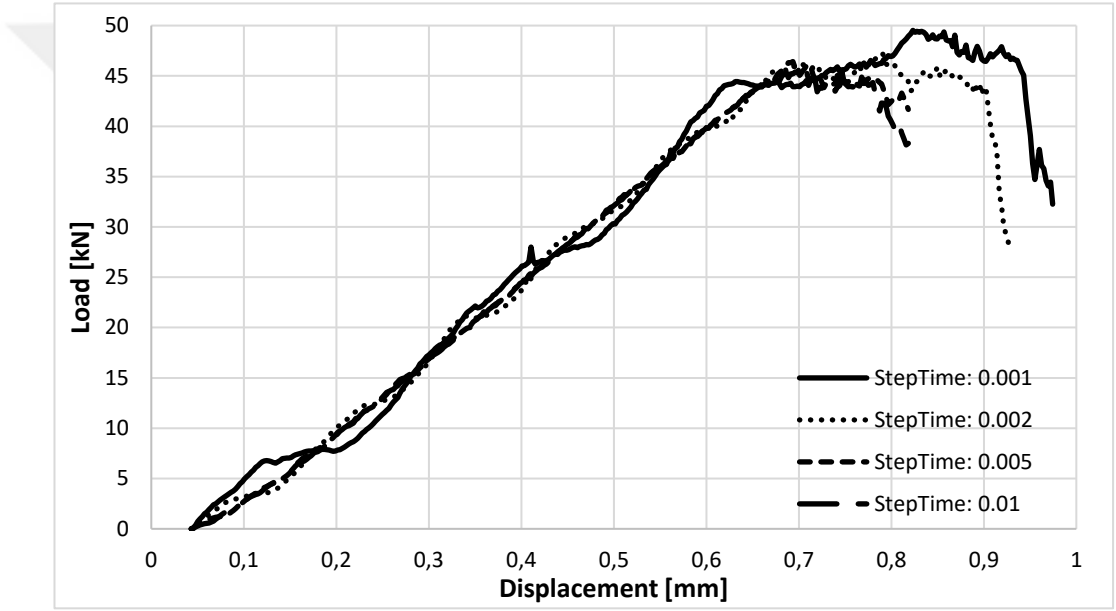

Figure 56: Load versus displacement graph of the analyses with different step times

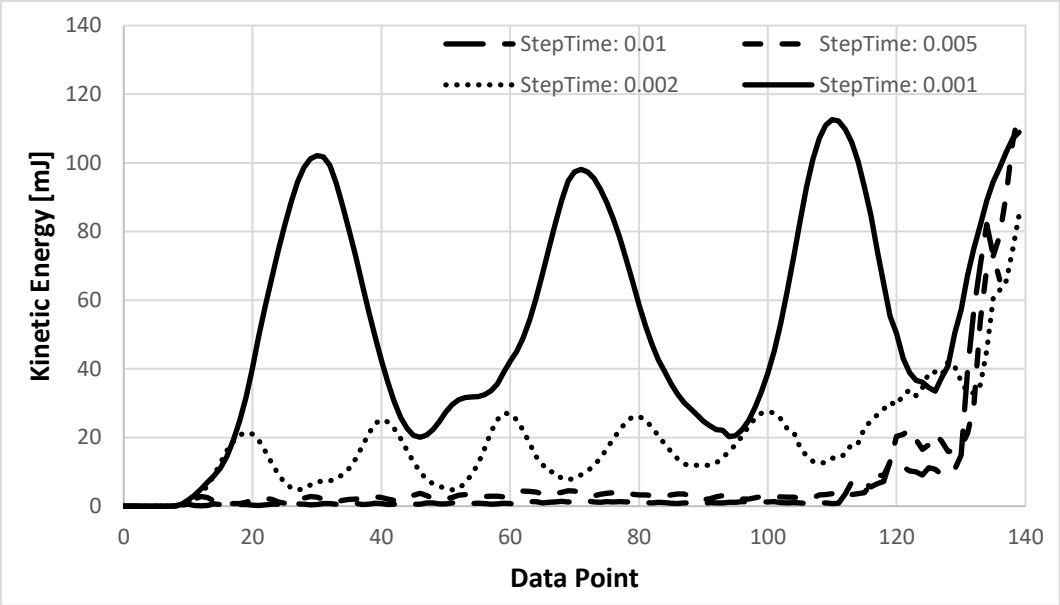

Figure 57: Kinetic energy graph of the analyses for different time steps

Another variable to define step is time increment. Abaqus™/Explicit calculates the required time increment by considering the material properties and element geometry to get stable results, but there is also a fix time increment option. Required time increment is calculated with following formula [48].

$$\Delta t \leq \min\left(L_e \sqrt{\frac{\rho}{\hat{\lambda} + 2\hat{\mu}}}\right) \tag{51}$$

where L_e is the characteristic length of the element, and $\hat{\lambda}$ and $\hat{\mu}$ are the effective Lame constants given as follows:

$$\hat{\lambda} = \frac{E\nu}{(1+\nu)(1-2\nu)} \tag{52}$$

$$\hat{\mu} = \frac{E}{2(1+\nu)} \tag{53}$$

4.6 Composite Lay-Up

For the modeling of nineteen layers, composite lay-up option of Abaqus™ is used. Since the lay-up is symmetric at the middle, nine normal layers and one half-thickness layer is assigned to the plate. Global coordinate system of the software is used so, the z-axes is chosen as the normal of the plate and the stacking direction; and the x-axes is set for the 0° orientation. A presentation of the stacking is shown in Figure 58.

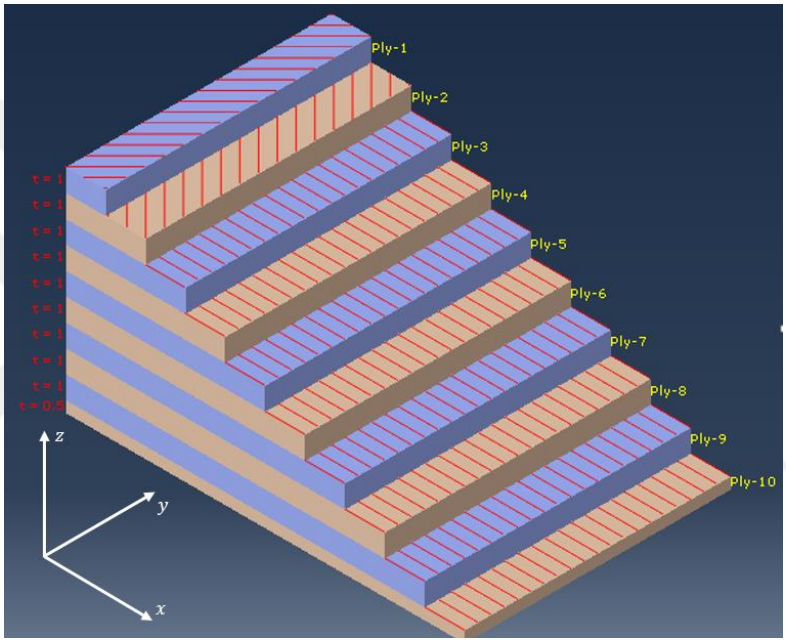

Figure 58: Stacking of the composite lay-up

Integration point for each ply can be determined as assigning composite lay-up. By default, Abaqus™ uses three integration points and in the manual [52] numbering of the integration points is given as in Figure 59.

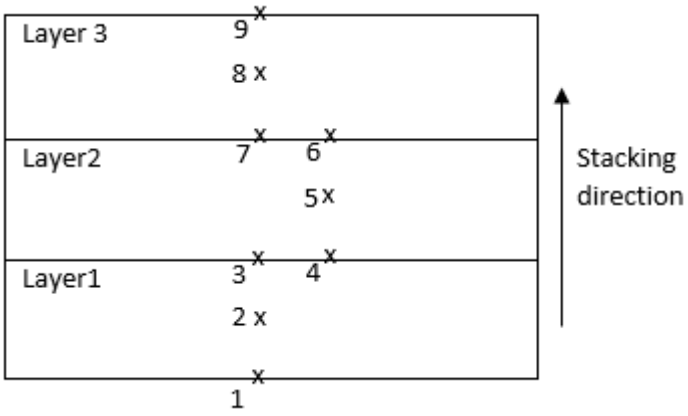

Figure 59: Numbering of integration points

4.7 Boundary Conditions

For simulation, four boundary conditions are created in the model. First boundary condition is assigned to hold the plate. An x-symmetry condition is assigned to the surface which constraints displacement in x-direction and rotations in y and z-directions. Second boundary condition satisfies the symmetry of mid-section of the plate. So, to the surface, which corresponds to outer surface of the layer ten, a z-symmetry condition is assigned which constraints displacement in z-direction and rotations of x and y-directions. Third and fourth ones are assigned on the pin. While the conditions are assigned on the surfaces for plate, they are assigned on the reference point which is defined on the pin. Third boundary condition constraints the pin except from x-displacement; while the last one defines a constant speed displacement in x-direction. These boundary conditions are presented in Figure 60.

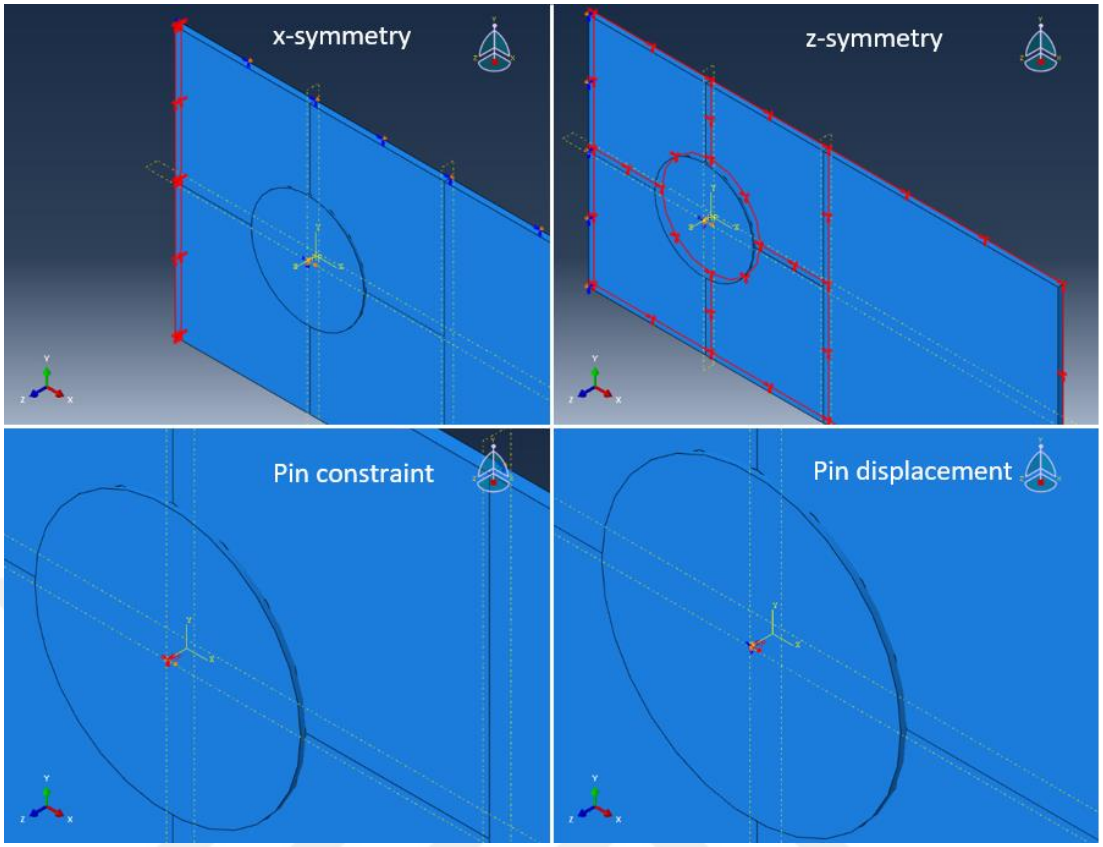

Figure 60: Boundary conditions

4.8 Cohesive Section

In order to examine delamination, cohesive layers are implemented to the model. According to zero thickness approach, 0.001 mm thickness is assigned to the layers.

In Figure 61, implemented cohesive layer between plies is presented. As seen in the figure, thickness of the cohesive layers is significantly smaller than the plies; in order not to affect bulk properties of the structure.

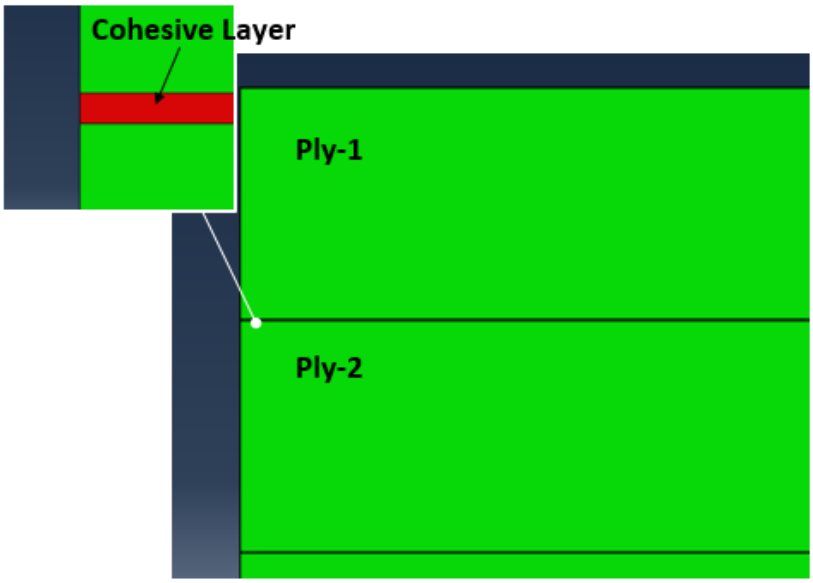

Figure 61: Cohesive layer in the finite element model

As explained in Chapter 2, the stiffness of cohesive layer must be assigned such that, it should not cause any artificial compliance due to cohesive interface. If the FRP is assumed as transversely isotropic, then $E_2 = E_3$. With these assumptions and using the model proposed by Turon et al. [24] stiffness of the interface is calculated as $K = 2.3 \cdot 10^6\ MPa$. Camanho et al. [17], shows that a stiffness in the order of $10^6\ MPa$ gives accurate results for delamination models. For the strength parameters, properties of the matrix which are determined by coupon tests are used. Then, Mode-I and Mode-II fracture energies which are determined by DCB and ENF tests, are assigned to predict crack propagation.

Another important parameter that effects the prediction capability of the model is the cohesive zone length, l_cz; which is the distance from the crack tip to the maximum traction point as shown in Figure 62.

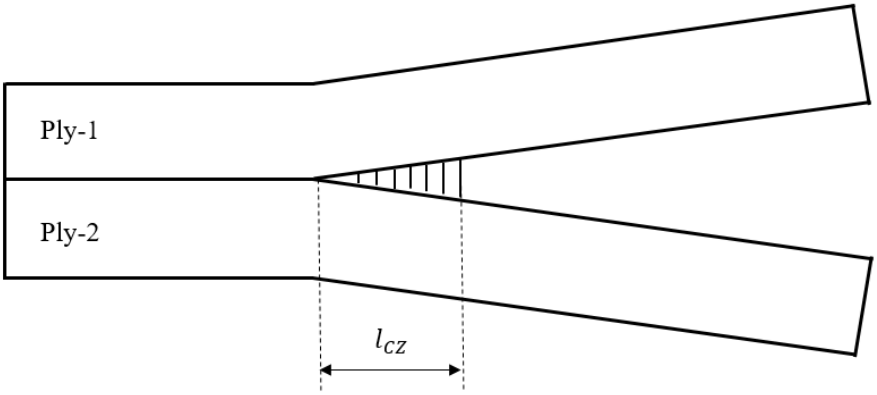

Figure 62: Cohesive zone length

Turon et al. [23], proposes a formula which predicts cohesive zone length as follows:

$$l_{cz} = ME\frac{G_c}{(\tau_0)^2} \tag{54}$$

where, E is the Young modulus, and G_c is the fracture energy release rate. M is a parameter which is close to unity and Hillerborg et al. [53] suggested that $M = 1$.

Turon et al. [23] propose that at least two elements should be in cohesive region, and if the required element size is too small than cohesive zone length can be increased by increasing the strength of interface. By that way, strength values are determined such that $l_{cz} = 1.5\ mm$.

Then a traction separation cohesive layer is modelled with the properties given in Table 12.

Table 12: Cohesive layer properties

Stiffness, K $[MPa]$	$2.3 \cdot 10^6$
Normal Strength, t_n^0 $[MPa]$	45
Shear Strength, t_s^0 $[MPa]$	57
Mode-I Fracture Energy, G_{Ic} $[N/mm]$	0.3
Mode-II Fracture Energy, G_{IIc} $[N/mm]$	0.47
Cohesive Zone Length, l_{cz} $[mm]$	1.5

Under the light of these information, two different models are built with/out cohesive layer. Analysis are run on a desktop computer with Intel® Core™ i7 3.20 GHz processor which uses eight cores. The computer also has 16 GB installed memory (RAM). Number of the elements in model and approximate run times of the analysis are given in Table 13.

Table 13: Finite element models

	Number of Elements	**Run Time**
Model with cohesive layer	123804	20 Hours
Model without cohesive layer	6824	6 Hours

CHAPTER 5

RESULTS

In this section, results of the models, with/out cohesive layer, are compared. Both of the models are analyzed with three progressive failure cases that are mentioned in Chapter 4. Result of the models are also compared with experimental results.

To be able to attach the specimens to the test machine easily, a two pinned plate is used for testing. The specimen is shown in Figure 63. The pins are placed to the holes without fastening and attached to the apparatus. The apparatus is used for connection between the grips of test machine and the pins. Displacement control test is performed with $0.5\ mm/s$ constant head speed.

Figure 63: Weight-pocket specimen

The plate has $600\ mm$ length and the distance from center of the hole to the edges is $150\ mm$. Since, modelling of whole plate requires too long run time, only a portion of the plate is modelled as explained in Chapter 4.

Five specimens are tested and the test results are given in Figure 64. From the results it is observed that maximum load is measured between $46.4\ kN$ and $52.8\ kN$. Average of the maximum loads is $50.5\ kN$. Since the plate is not modeled as a whole and deformation is observed differently at the holes, displacement does not give an idea about the predictive capability of the numerical analysis.

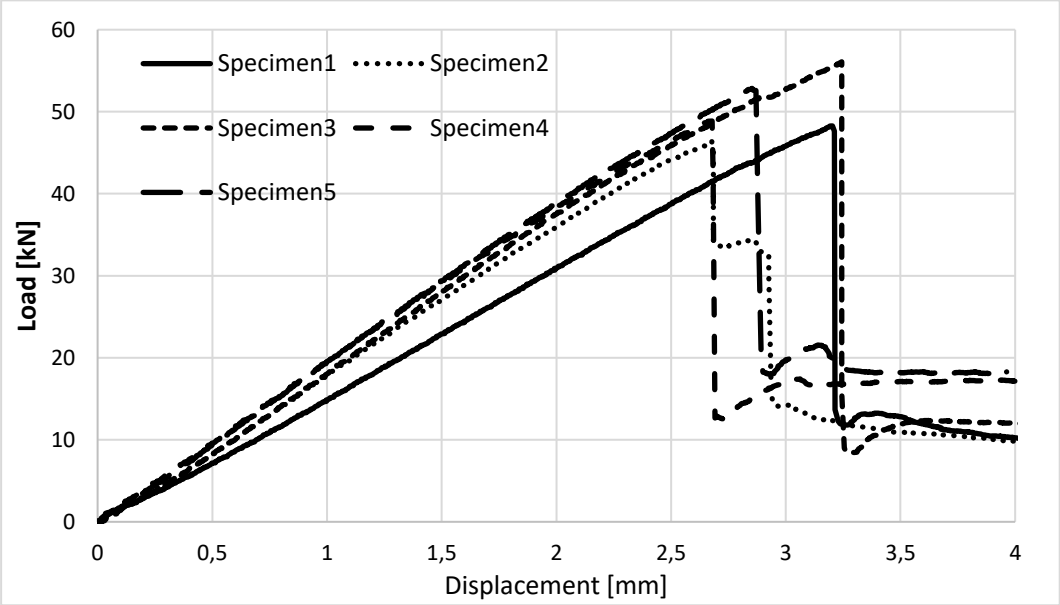

Figure 64: Load versus displacement graph of the experiment

Another measure to compare the model and the experiment is to examine failure type and where it occurs. In Figure 65, failure location of the specimen is shown under the light. Light helps to see failure inside the plate. Opaque regions are the delamination, and the matrix failure is seen as lines inside the layers. So, delamination is observed in a wide region. Matrix failure is seen for layers with $45°, -45°, 0°$ fiber orientations; and fiber failure is visible for the first ply. Fiber failure is the cause of final failure at the ultimate point, and the reason is the load carrying capacity of the fibers.

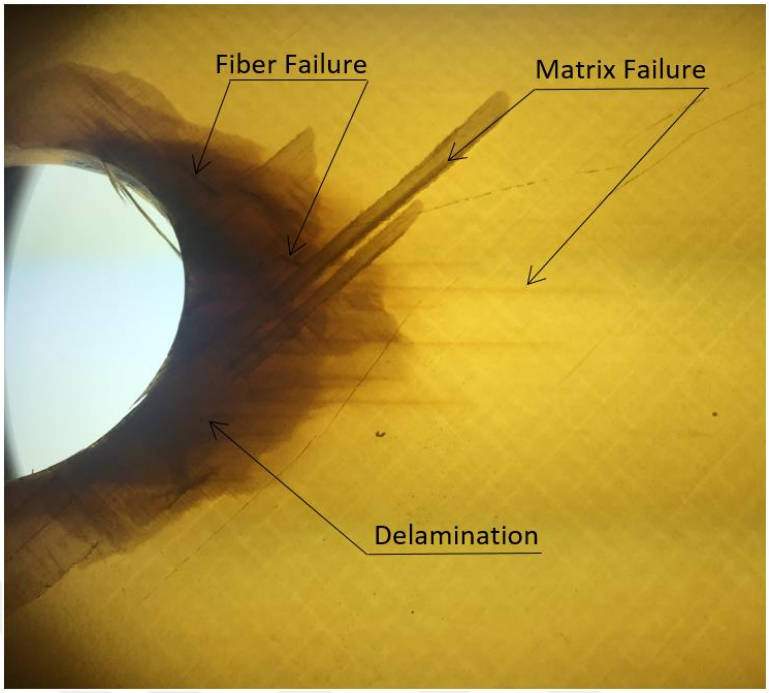

Figure 65: Failure region

For numerical analysis, first the model without cohesive layer is used. Analyses are done for the progression cases which are explained in Chapter 4. In Figure 66, the analyses results are presented. For Case 1 ultimate load is $43.9\,kN$, for Case 2 $54.1\,kN$, and for Case 3 $60.1\,kN$. Since these models are not considering delamination, ultimate load is expected higher than experimental result. Case 2 and 3 are logical in this manner; on the other hand, Case 1 gives very conservative result.

For Case 2, failure type and region is examined in Figure 67. Just before the final failure, total compressive failure of matrix is observed. Matrix tensile failure is seemed to be initiated but the elements still carries load. On the other hand, there is not any damage at fibers. When the ultimate load is reached, load decreases suddenly with the initiation of fiber compressive failure. The plate just after the failure is shown in Figure 68. This results is consistent with the experiment, since the fiber compression is the reason of final failure.

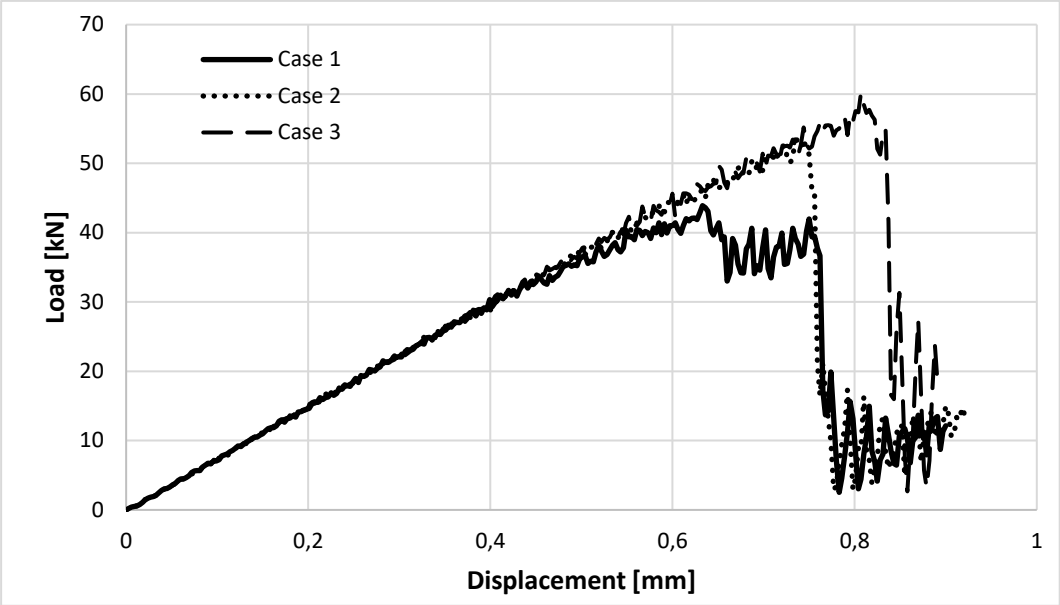

Figure 66: Load versus displacement graph of the analyses results (without cohesive layer)

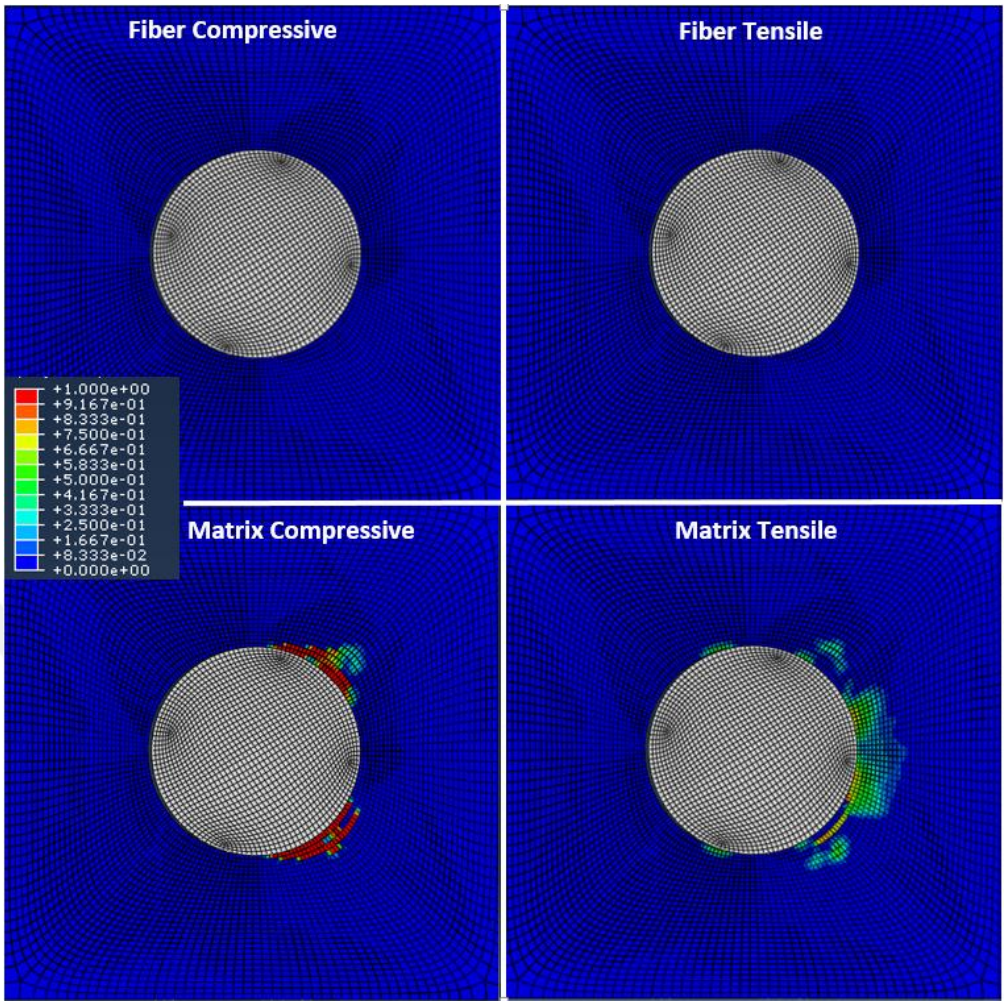

Figure 67: Failure at ultimate load

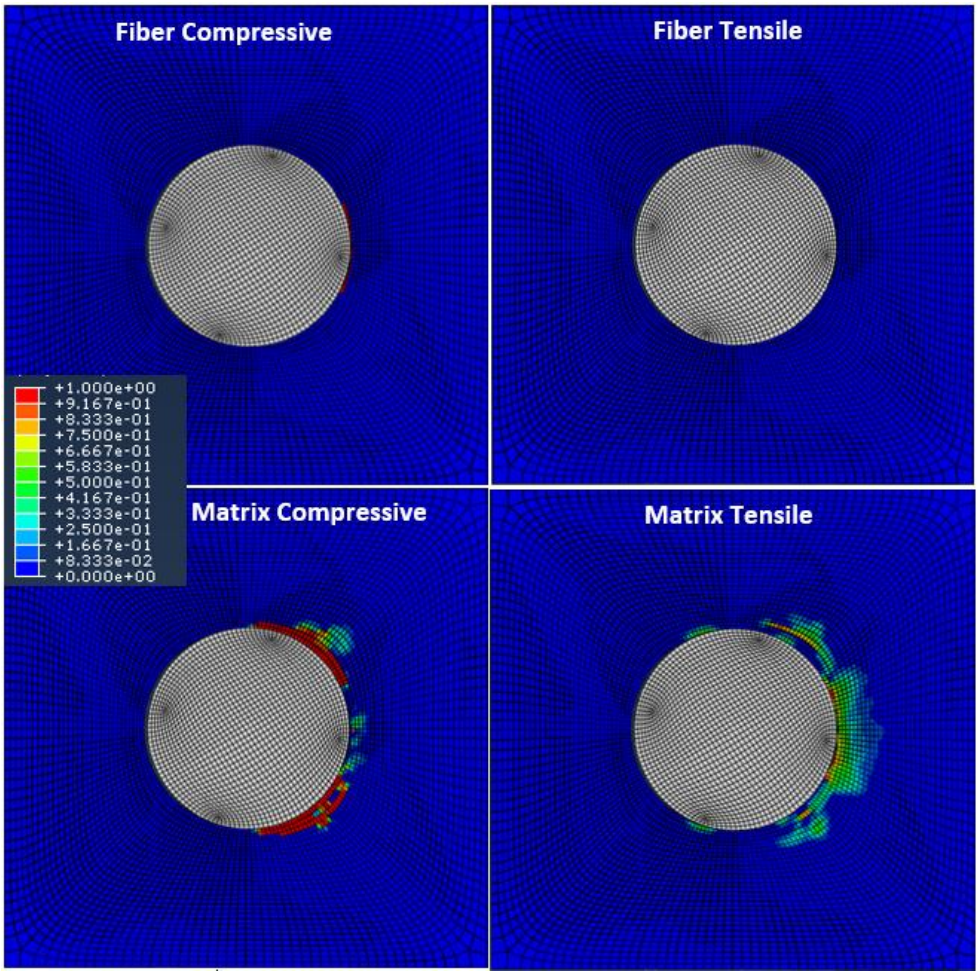

Figure 68: Failure after the ultimate load

After obtaining logical results with the model, CZM is implemented and effect of the delamination is examined. Force versus displacement graph of the analysis with cohesive layer for three cases is given in Figure 69. Ultimate loads are determined as $41.5\ kN, 53.6\ kN$, and $59.4\ kN$ for Case 1, 2, and 3, respectively. These ultimate loads are slightly lower than the results of without cohesive layer analysis. This is an expected result since the delamination causes loss in stiffness and triggers failure. Case 2 model predicts ultimate load with less than 2% error.

Again Case 2 is investigated for failure type and region. As seen in Figure 70, delamination is observed between $+45°/-45°$ and $-45°/0°$. There is not any delamination between 0° layers as expected.

Figure 69: Force versus displacement graph of the analysis results (with cohesive layer)

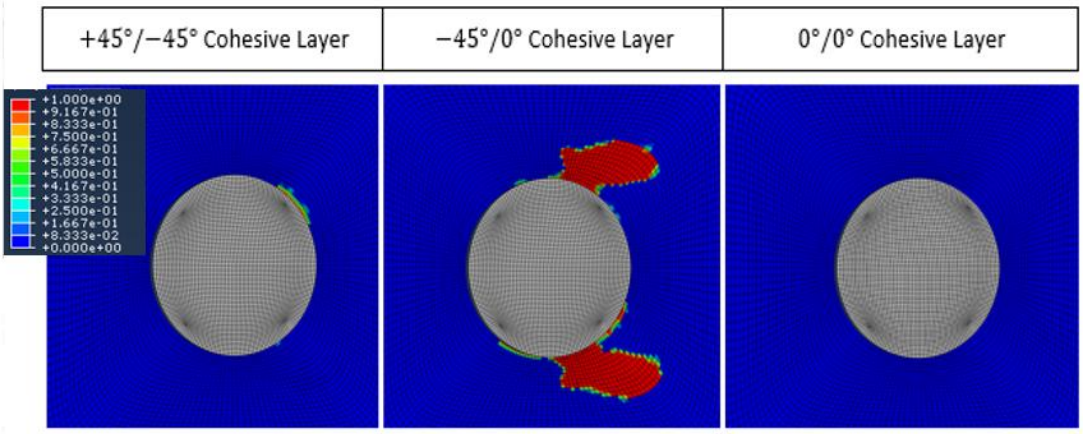

Figure 70: Delamination failure before the ultimate load

At this load, matrix failure for composite lay-up is given in Figure 71. Tensile and compressive failure is observed for $\pm 45°$ layers in a symmetric case. However, only compressive matrix failure is observed in $0°$ plies. These matrix failure regions are clearly seen in Figure 65. For this load, there is not any failure observed in fibers. When the ultimate load is reached, fiber fails compressively in the third ply and load

drops. Fiber compressive failure is shown in Figure 72. This compressive failure region also agrees with the experimental investigations.

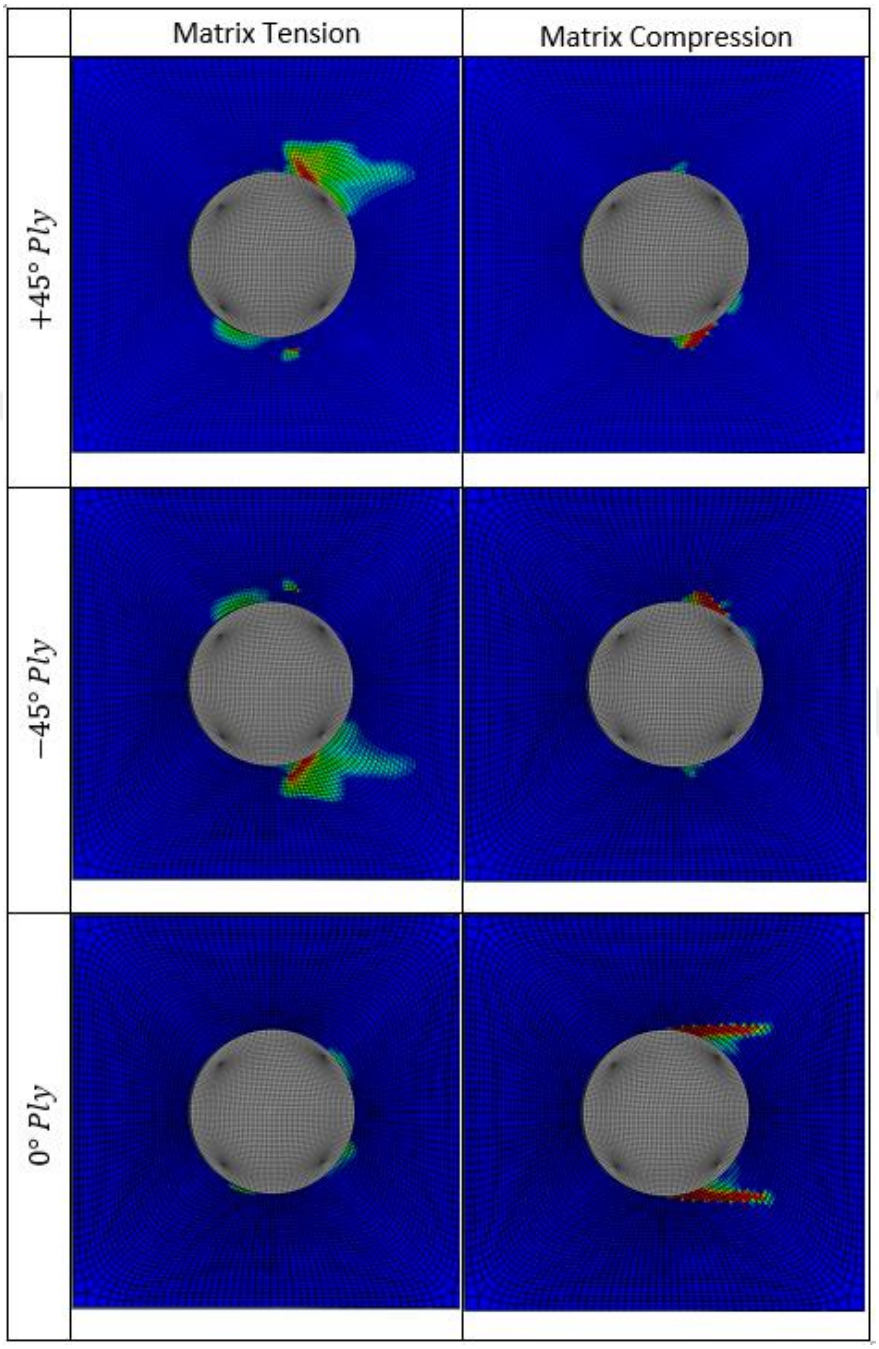

Figure 71: Matrix failure of composite plies before ultimate load

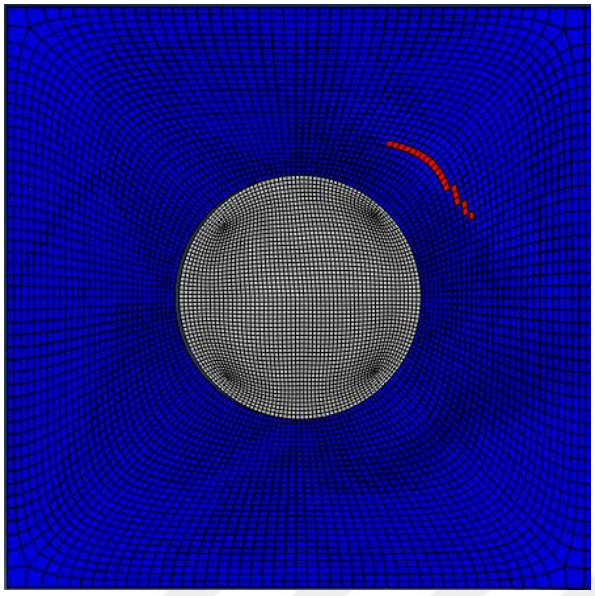

Figure 72: Fiber compressive failure after the ultimate load (Ply-3)

Numerical analyze is completed with these comparisons, and good prediction of the failure. Results are presented and compared with each other to have a good understanding of the model. Experimental results are used for validation of the results.

CHAPTER 6

DISCUSSION AND FUTURE WORK

In this thesis, a design methodology study is presented range from the experimental material characterization to the validation of the numerical model using the experimental data.

Material characterization is an important part of this work, since it gives experience for testing, and material properties are obtained.

For the finite element model, Abaqus™ is used and models with/out CZM are built. By literature review and comparing models with different mesh and step time, an optimum parameters are determined for the simulation. Then the substructure, weight-pocket, is modelled and ultimate load that the structure carries is determined. For progressive failure different cases are compared to find the best degradation model.

Then the experiments are conducted for the validation of model. The plate which simulates a region of the helicopter blade, is loaded at the holes. Load and displacement data is recorded with $5\,Hz$. Failure is observed sudden load drop as presented in Chapter 5. Ultimate load and failure type is compared with numerical results.

From the results it is clearly seen that, sudden failure model gives too conservative results and predicts ultimate load around 20% lower than experimental one. For the gradual failure models, Case 2 gives the closest results with the experiments. Predicting ultimate load with less than 2% error, and matching failure type and region validates the model.

Including delamination with CZM, results in load drop as expected. However, this load change is less than 2%. This result shows that delamination is not the major failure mechanism for this structure. Both experiment and numerical analyze show that fiber compression is the cause of final failure. Energy release rate of the fiber verifies this result.

Results shows that, there is not any delamination between 0° plies; so cohesive layers between them can be removed from the model and by that way running time can be reduced significantly.

As the future work, first, this methodology should be verified with different structures and according to obtained results finite element model can be improved.

Second, different failure criteria should be implemented. Abaqus™ uses Hashin criterion, however, as explained in Chapter 2, this criterion is not appropriate especially for compressive cases. Puck or LaRC criteria can be implemented to the software by a sub-routine to determine optimum criterion.

Third, gradual failure progression should be investigated further. Finite element models can be built for coupon bearing and fracture toughness tests (DCB and ENF) and more accurate energy release rates can be obtained by that way. Similar approach is followed by Camanho et al. [17].

REFERENCES

[1] V. V. Vasiliev and E. V. Morozov, *Advanced mechanics of composite materials and structural elements,* Third. Oxford: Elsevier Ltd, 2013.

[2] R. M. Jones, *Mechanics of composite materials*, Third. London: Taylor & Francis, 1998.

[3] "1001 Crash - Composite made commercial airplane." [Online]. Available: http://www.1001crash.com/index-page-composite-lg-2.html.

[4] R. Talreja, "Assessment of the fundamentals of failure theories for composite materials," *Compos. Sci. Technol.*, vol. 105, pp. 190–201, 2014.

[5] M. J. Hinton, a S. Kaddour, and P. D. Soden, "The world-wide failure exercise : Its origin , concept and content," pp. 2–28, 2004.

[6] a. S. Kaddour, M. J. Hinton, and P. D. Soden, "Predictive capabilities of nineteen failure theories and design methodologies for polymer composite laminates. Part B: Comparison with Experiments," *... Polym. Compos. World-Wide Fail. ...*, 2004.

[7] P. Nali and E. Carrera, "A numerical assessment on two-dimensional failure criteria for composite layered structures," *Compos. Part B Eng.*, vol. 43, no. 2, pp. 280–289, 2012.

[8] R. Hill, "A theory of the yielding and plastic flow of anisotropic metals," *Math. Phys. Sci.*, vol. 193, no. 1033, pp. 281–297, 1948.

[9] V. D. Azzi and S. W. Tsai, "Anisotropic strength of composites - Investigation aimed at developing a theory applicable to laminated as well as unidirectional composites, employing simple material properties derived from unidirectional specimens alone," *Exp. Mech.*, vol. 5, no. 9, pp. 283–288, 1965.

[10] K. K. Chawla, *Composite materials*, 3rd ed. New York: Springer-Verlag, 1985.

[11] Z. Hashin, “Failure Criteria for Unidirectional Fiber Composites,” *J. Appl. Mech.*, vol. 47, no. 2, p. 329, 1980.

[12] a. Puck and H. Schürmann, “Failure analysis of FRP laminates by means of physically based phenomenological models,” *Compos. Sci. Technol.*, vol. 62, no. 12–13 SPECIAL ISSUE, pp. 1633–1662, 2002.

[13] A. Puck, J. Kopp, and M. Knops, “Guidelines for the determination of the parameters in Puck’s action plane strength criterion,” *Compos. Sci. Technol.*, vol. 62, no. 3, pp. 371–378, 2002.

[14] C. G. Davila, P. P. Camanho, and C. A. Rose, “Failure Criteria for FRP Laminates,” *J. Compos. Mater.*, vol. 39, no. 4, pp. 323–345, 2005.

[15] S. T. Pinho, C. G. Dávila, P. P. Camanho, L. Iannucci, and P. Robinson, “Failure Models and Criteria for FRP Under In-Plane or Three-Dimensional Stress States Including Shear Non-linearity,” *Tm-2005-213530*, no. February, p. 68, 2005.

[16] P. D. Soden, a. S. Kaddour, and M. J. Hinton, “Recommendations for designers and researchers resulting from the world-wide failure exercise,” *Compos. Sci. Technol.*, vol. 64, no. 3–4, pp. 589–604, 2004.

[17] P. Camanho, C. G. Davila, and M. F. De Moura, “Numerical Simulation of Mixed-mode Progressive Delamination in Composite Materials,” *J. Compos. Mater.*, vol. 37, pp. 1415–1438, 2003.

[18] G. Alfano and M. A. Crisfield, “Finite element interface models for the delamination analysis of laminated composites: Mechanical and computational issues,” *Int. J. Numer. Methods Eng.*, vol. 50, no. 7, pp. 1701–1736, 2001.

[19] R. Krueger, “Virtual crack closure technique: History, approach, and applications,” *Appl. Mech. Rev.*, vol. 57, no. 2, p. 109, 2004.

[20] Q. Yang and B. Cox, “Cohesive models for damage evolution in laminated composites,” *Int. J. Fract.*, vol. 133, pp. 107–137, 2005.

[21] J. R. Rice, “A Path Independent Integral and the Approximate Analysis of Strain

Concentration by Notches and Cracks," *J. Appl. Mech.*, vol. 35, no. 2, p. 379, 1968.

[22] D. M. Parks, "A stiffness derivative finite element technique for determination of crack tip stress intensity factors," *Int. J. Fract.*, vol. 10, no. 4, pp. 487–502, 1974.

[23] A. Turon, C. G. Dávila, P. P. Camanho, and J. Costa, "An Engineering Solution for Solving Mesh Size Effects in the Simulation of Delamination with Cohesive Zone Models," no. June 2005, 2005.

[24] A. Turon, C. G. Dávila, P. P. Camanho, and J. Costa, "An Engineering Solution for using Coarse Meshes in the Simulation of Delamination With Cohesive Zone Models," *Nasa/Tm-2005-213547*, no. March, pp. 1–26, 2005.

[25] S. W. Tsai, *Theory of Composites Design*. Dayton, Ohio: Think Composites, 1992.

[26] K. S. Liu and S. W. Tsai, "A progressive quadratic failure criterion for a laminate," *Compos. Sci. Technol.*, vol. 58, no. 7, pp. 1023–1032, 1998.

[27] A. Matzenmiller, J. Lubliner, and R. L. Taylor, "A constitutive model for anisotropic damage in fiber-composites," *Mech. Mater.*, vol. 20, no. 2, pp. 125–152, 1995.

[28] P. Maimí, P. P. Camanho, J. A. Mayugo, and C. G. Dávila, "A continuum damage model for composite laminates: Part I - Constitutive model," *Mech. Mater.*, vol. 39, no. 10, pp. 897–908, 2007.

[29] D. W. Sleight, "Progressive Failure Analysis Methodology for Laminated Composite Structures," *Nasa/Tp-1999-209107*, no. March, 1999.

[30] M. R. Garnich and V. M. K. Akula, "Review of Degradation Models for Progressive Failure Analysis of Fiber Reinforced Polymer Composites," *Appl. Mech. Rev.*, vol. 62, no. 1, p. 10801, 2009.

[31] Y. S. N. Reddy and J. N. Reddy, "Three-dimensional finite element progressive failure analysis of composite laminates under axial extension," *J. Compos.*

Technol. Res., vol. 15, no. 2, pp. 73–87, 1993.

[32] I. Lapczyk and J. A. Hurtado, "Progressive damage modeling in fiber-reinforced materials," *Compos. Part A Appl. Sci. Manuf.*, vol. 38, no. 11, pp. 2333–2341, 2007.

[33] Abaqus Inc, "Analysis user's guide Chapter 24.3," no. 6.14, p. 294, 2014.

[34] P. Maimí, P. P. Camanho, J. A. Mayugo, and C. G. Dávila, "A Thermodynamically Consistent Damage Model for Advanced Composites. NASA/TM-2006-214282," *Nasa Tm*, no. March, p. 47, 2006.

[35] S. T. Pinho, "Modelling failure of laminated composites using physically-based failure models," 2005.

[36] Z. P. Bazant, J.-J. H. Kim, I. M. Daniel, E. Becq-Giraudon, and G. Zi, "Size Effect on Compression Strength of Fiber Composites Failing by Kink Band Propagation," *Int. J. Fract.*, vol. 95, no. Bažant 1984, pp. 103–141, 1999.

[37] ASTM INTERNATIONAL, "ASTM D3039/D3039M: Standard test method for tensile properties of polymer matrix composite materials," *Annu. B. ASTM Stand.*, pp. 1–13, 2014.

[38] DIN, "DIN EN 2850 Aerospace series carbon fibre thermosetting resin unidirectional laminates compression test parallel to fibre direction," 1998.

[39] ASTM INTERNATIONAL, "ASTM D3518/D3518M Standard Test Method for In-Plane Shear Response of Polymer Matrix Composite Materials by Tensile Test of a 645 ° Laminate 1," *Annu. B. ASTM Stand.*, vol. 94, no. Reapproved, pp. 1–7, 2007.

[40] ASTM INTERNATIONAL, "ASTM D5766/D5766M Standard Test Method for Open-Hole Tensile Strength of Polymer Matrix Composite," *Annu. B. ASTM Stand.*, pp. 1–7, 2013.

[41] DIN, "DIN EN 6036 Aerospace series fibre reinforced plastics test method determination of notched, unnotched and filled hole compression strength," 1996.

[42] ASTM INTERNATIONAL, “ASTM D5961/D5961M Standard Test Method for Bearing Response of Polymer Matrix Composite Laminates,” *Annu. B. ASTM Stand.*, vol. i, no. April 2004, pp. 1–18, 2003.

[43] R. Smith, “Composite Defects and Their Detection,” *Mater. Sci. Eng.*, vol. III, p. 14, 1997.

[44] M. Patrıcio and R. Mattheij, “Crack propagation analysis,” *CASA Rep.*, 2007.

[45] ASTM INTERNATIONAL, “D5528-01 2001. Standard Test Method for Mode I Interlaminar Fracture Toughness of Unidirectional Fiber-Reinforced Polymer Matrix Composites,” *Annu. B. ASTM Stand.*, no. Mode I, pp. 1–13, 2014.

[46] ASTM INTERNATIONAL, “ASTM D7905/D7905M Standard Test Method for Determination of the Mode II Interlaminar Fracture Toughness of Unidirectional Fiber-Reinforced Polymer Matrix Composites,” *Annu. B. ASTM Stand.*, vol. 15.03, pp. 1–18, 2014.

[47] E. J. Barbero, *Finite Element Analysis of Composite Materials*. Boca Raton: CRC Press, 2008.

[48] Abaqus Inc, “Analysis user’s guide Chapter 6.3,” no. 6.14, 2014.

[49] Abaqus Inc, “Abaqus/CAE user’s guide Chapter 12.14,” no. 6.14, 2014.

[50] Abaqus Inc, “Analysis user’s guide Chapter 29.6,” no. 6.14, 2014.

[51] Abaqus Inc, “Abaqus Theory Guide Chapter 2.4,” no. 6.14, 2014.

[52] Abaqus Inc, “Abaqus/CAE user’s guide Chapter 23.5,” no. 6.14, 2014.

[53] A. Hillerborg, M. Modéer, and P.-E. Petersson, “Analysis of crack formation and crack growth in concrete by means of fracture mechanics and finite elements,” *Cem. Concr. Res.*, vol. 6, no. 6, pp. 773–781, 1976.